Microstructure-informed, predictive crystal plasticity finite element model of fatigue-dwells

Dylan Agius[a], Abdullah Al Mamun[a], Chris A Simpson[a], Christopher Truman[a], Yiqiang Wang[b], Mahmoud Mostafavi[a] and David Knowles[a]

[a]Solid Mechanics Research Group, Department of Mechanical Engineering, University of Bristol, Bristol BS8 1TR, UK

[b]United Kingdom Atomic Energy Authority, Culham Science Centre, Abingdon OX14 3DB, UK

Abstract

Crystal plasticity finite element (CPFE) modelling is an effective tool from which detailed information on the meso-scale behaviour of crystalline metallic systems can be extracted and used, not only to enhance the understanding of material behaviour under different loading conditions, but also to improve the structural integrity assessment of engineering components. To be of full benefit however it must be demonstrated to not only predict the average global response of the material, but also the local behaviour, to provide insight into localised regions of stress and plastic strain. In this study, a slip system based constitutive model is developed to improve the simulation capability of time independent and time dependent plasticity. Comparison has been made between the macro-mechanical behaviour predicted by the model and previous experiments carried out at engineering length scale. Critically, the macro-mechanical behaviour predicted by the model has been examined against the behaviour of the materials at the meso-scale crystalline level measured by previous diffraction experiments. The robustness of the model is demonstrated on both the macro- and meso-scale through the successful prediction of macro-scale behaviour and lattice strain evolution under a variety of loading conditions. The model not only effectively recognised the influence of prior deformation on subsequent loading, but also complemented neutron diffraction data to enrich the understanding of the influence of an important loading condition on the deformation of grains within the material.

Key words: Crystal plasticity, Stress relaxation, Stainless Steel, Plasticity, Creep, Intragranular Stress

1. Introduction

Since complex thermomechanical loading is expected during operation of a power plant, it is vitally important to not only understand the influence of these complex load histories on the life of components, but also on the micro-mechanisms within their materials. Doing so provides an improved understanding of the deformation of material in the components, but critically a greater insight into the influence of the micromechanics. This also allows for the enhanced evaluation of more suitable materials for future design and construction of components.

Computational materials engineering using crystal plasticity finite element (CPFE) modelling can provide aspects of insight into the behaviour of the crystalline material when subject to complex

load histories. The recognition of this approach to integrate CPFE into the design of materials has been gaining popularity through the emergence of integrated computational materials engineering (ICME) methodologies over the last few years. It has also been fuelled by the drive to integrate the processing-microstructure-property-relationships in the design process of materials. Recent examples of the success of ICME approaches include the work by Tin, et al. [1] who used ICME to modify a Ni-based superalloy to improve its damage-tolerance. In addition, CPFE approaches have also been utilised to extract deeper insight into the local deformation of the material which is on occasion difficult to obtain experimentally, an approach utilised by Tasan, et al. [2] to compliment experimental data in the investigation of microstructural strain and stress partitioning in ferritic-martensitic dual phase steels. Furthermore, Sinha, et al. [3] used CPFE, in conjunction with electron backscatter diffraction data, to develop deeper understanding around the influence of twinning during tensile loading of 316L stainless steel.

There are a number of different phenomena which can affect the life of metallic components exposed to complex thermo-mechanical loading history. These include time-dependent permanent deformation such as strain accumulation and stress relaxation occurring during creep. Both strain accumulation and stress relaxation can occur during plant operation due to loading conditions which induce either load or displacement-controlled deformation or a combination of both. Therefore, it is important to develop an understanding of how these phenomena evolve to provide greater insight on their influence on the life of components within the plant. Such an approach was used by Song, et al. [4] in development of a ferritic alloy with improved creep resistance, achieved through the findings associated with the integration of advanced experimental tools (including transmission-electron microscopy, neutron diffraction, and atom-probe tomography) and CPFE. The creep resistance was enhanced through the inclusion of coherent hierarchical precipitates, the influence of which was quantified through the integration of these different tools.

Further development in understanding has also extended to consideration of the influence of cyclic loading on creep deformation. Cyclic deformation can occur due to periodic shutdowns and scheduled maintenance [5]. The influence of the generated cyclic deformation on creep in austenitic stainless steels from a macro-scale deformation has been investigated experimentally, with the findings indicating that the evolution of creep strain and stress relaxation can be affected by prior cyclic loading [6-8]. Additionally, experimental investigation on the local level using neutron diffraction has also been conducted by [9-12] to provide greater insight into the contribution of intergranular stresses generated during cyclic loading on the creep deformation. These studies have highlighted the differences in grain-to-grain interactions occurring during plasticity and creep resulting in different levels of anisotropy. This additional experimental investigation is vital in generating a more detailed insight of the underlying micromechanics of deformation which contribute to the macro-scale deformation.

To complement the experimental investigation into creep and prior cyclic loading on creep, there has been a significant push towards using micromechanical models, which include self-consistent models (SCM) [13] and CPFE. SCM have been used to simulate the deformation of austenitic stainless steels subject to different loading conditions. Stress relaxation and creep for short dwell periods was investigated by Wang, et al. [14] using a combination of neutron diffraction and SCM.

Good agreement was achieved in both macro- and meso-scale simulations for the short dwells. Improvements to SCM simulations for creep were made by Hu, et al. [15] in the investigation on the effect of creep strain on the Bauschinger effect. Additionally, the effect of thermal aging on creep deformation was investigated by Chen, et al. [16] and Wang, et al. [17] who considered the influence of martensitic phase transformation. Further modifications were also introduced by Petkov, et al. [5] to improve the SCM capabilities to simulate macroscopic stress relaxation, creep strain evolution, and the influence of prior cyclic loading on creep.

In addition to the investigation of austenitic stainless steels using SCM, CPFE has also grown in popularity to provide in depth knowledge of the structural integrity of the material. The focus of this understanding has included damage evolution and crack initiation [18-21], influence of grain morphology and orientation on local deformation [22, 23], lattice strain evolution [18, 24-28] and low-cycle fatigue [29]. CPFE has also been applied to investigate the evolution of creep strain. Petkov, et al. [30] used a CPFE model to simulate the evolution of creep strain, which was then compared to the predictions made using a SCM modelling approach. Additionally, Erinosho, et al. [31] investigated the influence of prior cyclic plastic loading on creep strain and introduced a modification to constitutive model controlling slip hardening to improve the deformation during the creep regime. Although CPFE modelling has been applied to understand the creep deformation under load-control dwells in austenitic stainless steels, limited work has been undertaken to understand how the predictive capabilities of these constitutive models translate to displacement-control (stress relaxation) dwells. This is a particularly important investigation to undertake in the development of a CPFE modelling capability to develop a robust modelling approach proficient in recognising the differences in lattice strain evolution during both constant load- and strain-control dwells.

In this study, a crystal plasticity constitutive model for 316H stainless steel has been developed to predict the amount of expected stress relaxation during single and multiple load-displacement dwells using previous experimental data by Wang, et al. [32-34] and Mamun, et al. [9], [12]. The modifications made to the underlying constitutive models (superposition of power laws, addition of intragranular stress, and the addition of recovery to the developed hardening) and the justification for the modifications are detailed based on microscopic behaviours of the material. A parameter calibration scheme is also detailed to ensure application of the constitutive models to other materials. Finally, the CPFE (using a synthetically built microstructure) is used to provide deeper understanding on the influence of local grain environmental effects on the deformation of crystals by simulating the lattice strain evolution and comparing the results to an experimental investigation undertaken by Wang, et al. [34].

2. Constitutive Model Development for Crystal Plasticity Modelling

In the following sections the crystal plasticity governing equations will be introduced to provide background on how crystal deformation is calculated. The constitutive relationships adopted will then be given, followed by the modifications introduced to incorporate phenomenologically the microscopic behaviours (e.g. time dependent and time independent plasticity, and the associated hardening and recovery phenomena) occurring in the material.

2.1 Kinematics

The following kinematic theory is based on the work described in [35-38], the history of which was reviewed in [39]. The summary presented is also based on the work by Huang [40].

The total crystal deformation ($\boldsymbol{F}$) can be described based on the contributions of both the plastic and elastic deformations, using the assumption that the deformation gradient obeys a multiplicative decomposition as given in the following equation,

$$\boldsymbol{F} = \boldsymbol{F}^e \boldsymbol{F}^p \tag{1}$$

where $\boldsymbol{F}^p$ is the plastic deformation associated with crystallographic slip, and $\boldsymbol{F}^e$ is the elastic deformation associated with rigid body rotation and elastic stretching of the crystal lattice.

The velocity gradient can be calculated using the following,

$$\boldsymbol{L} = \dot{\boldsymbol{F}}\boldsymbol{F}^{-1} = \boldsymbol{D} + \boldsymbol{\Omega} \tag{2}$$

where $\boldsymbol{D}$ is the stretch tensor and $\boldsymbol{\Omega}$ the spin tensor respectively. These two tensors representing stretch and spin can themselves be decomposed into lattice and plastic parts (through application of the assumption of small elastic stretch),

$$\boldsymbol{D} = \boldsymbol{D}^e + \boldsymbol{D}^p, \quad \boldsymbol{\Omega} = \boldsymbol{\Omega}^e + \boldsymbol{\Omega}^p \tag{3}$$

where $\boldsymbol{D}^p$ and $\boldsymbol{\Omega}^p$ are plastic stretch tensor and plastic spin tensor respectively. These plastic tensors result from crystallographic slip which can be captured by the following relations,

$$\boldsymbol{D}^e + \boldsymbol{\Omega}^e = \dot{\boldsymbol{F}}^e \boldsymbol{F}^{e-1}, \quad \boldsymbol{D}^p + \boldsymbol{\Omega}^p = \sum_{\alpha=1}^{N_s} \dot{\gamma}^\alpha \boldsymbol{s}^{*\alpha} \otimes \boldsymbol{m}^{*\alpha} \tag{4}$$

where N_s is the number of slip systems, $\dot{\gamma}^\alpha$ is the slip rate on slip system α, $\boldsymbol{s}^{*\alpha}$ and $\boldsymbol{m}^{*\alpha}$ represents the vector along the slip direction and the vector representing the normal to the slip plane of system α in the deformed configuration respectively,

$$\boldsymbol{s}^{*\alpha} = \boldsymbol{F}^e \boldsymbol{s}^\alpha, \quad \boldsymbol{m}^{*\alpha} = \boldsymbol{m}^\alpha \boldsymbol{F}^{e-1} \tag{5}$$

where $\boldsymbol{s}^\alpha$ and $\boldsymbol{m}^\alpha$ are the unit vectors in the slip direction and normal to the slip plane in the reference configuration respectively.

2.2 Constitutive Models

Slip can be modelled using a visco-plastic power-law relation following the work by [41, 42],

$$\dot{\gamma}^\alpha = \dot{\gamma}_0 \left(\frac{\tau^\alpha}{g^\alpha} \right)^n sgn(\tau^\alpha) \tag{6}$$

where $\dot{\gamma}_o$ is a reference strain rate, τ^α is the resolved shear stress on the slip system α, g^α is a measure of the material's resistance to slip on the slip system α (which relates to strain hardening and/or softening) and n is a strain rate sensitivity parameter. Altering the value of n can reflect the sensitivity of the strain rate.

Slip system hardening can evolve according to a phenomenological based formulation of accumulated shear flow, which is an average plastic shear strain representing the overall effect

of dislocation movement [43]. The evolution adopted for this work is that proposed by Peirce, et al. [44]. This version of hardening model is based on the assumption made by Taylor [35] where all activated slip systems result in equal hardening across all slip systems. Therefore, the applied slip hardening model can be described as slip system isotropic hardening. The slip hardening has the following evolution,

$$\dot{g^{\alpha}} = h_0 \sum_{\beta=1}^{N_s} \left\{ \left(1 + \frac{h_0 \gamma_{sum}}{\tau_0 m} \right)^{m-1} \left| \dot{\gamma}^{\beta} \right| \right\} \tag{7}$$

where h_0 is the initial hardening modulus, m is a fitting parameter used to alter the rate of saturation, and τ_0 the initial critical resolved shear stress. γ_{sum} is the total accumulated inelastic shear strain on all slip systems which evolves according to Eq 8,

$$\gamma_{sum} = \sum_{\beta=1}^{N_s} \int_0^t \left| \dot{\gamma}^{\beta} \right| dt \tag{8}$$

2.3 Constitutive Model Modifications

In the following sections, the modifications made to the basic constitutive equations proposed in the previous sections are explained from a microstructure influence.

2.3.1 Intragranular stress

One of the benefits of CPFE method is it intrinsically incorporates the capability to generate intergranular stress associated with grain-to-grain kinematic effects [45]. However, to further improve the CPFE model it was found necessary to also include local intragranular stress into the constitutive model to recognise their influence on the deformation of the polycrystal as indicated by Hu, et al. [46]. To incorporate the intragranular stresses, the slip rate constitutive relation given in Eq 6 was modified to give the following,

$$\dot{\gamma}^{\alpha} = \dot{\gamma}_0 \left(\frac{|\tau^{\alpha} - X^{\alpha}|}{g^{\alpha}} \right)^n sgn(\tau^{\alpha} - X^{\alpha}) \tag{9}$$

X^{α} in Eq 9 is the intragranular stress, which in this study evolves according to the Armstrong-Fredrick (AF) model [47] expressed as,

$$\dot{X^{\alpha}} = h\dot{\gamma}^{\alpha} - h_D X^{\alpha} |\dot{\gamma}^{\alpha}| \tag{10}$$

where h is the direct hardening coefficient and h_D controls the dynamic recovery. The ratio of the values (h/h_D) controls the saturation level of X^{α} in each slip system [48], where X^{α} is evolving in the direction of $\dot{\gamma}$ as a scaler value based on the current amount of intragranular stress in the slip system. The inclusion of intragranular stress through an AF formulation is a phenomenological approach proposed by several researchers [49-51] but has since gathered even greater popularity.

The current formulation assumes that the evolution of the intragranular stress is dependent on slip within its own slip system, thus its evolution does not depend on slip on other systems. This is unlike the formulation proposed by Xu, et al. [52]. This approach was applied to ensure simplicity of application, since the current formulation requires only two calibrating parameters. Therefore, a simpler formulation of X^{α} was derived to provide a baseline for simulation and experimental comparisons.

2.3.2 Decomposing the Flow Rule

Creep can be caused by diffusion-controlled climb, which can be thought of as a two-step process as discussed by Duffin, et al. [53]. A slip plane containing dislocations restricted by obstacles can overcome the influence of the obstacle via climbing. Once doing so, the dislocations can then glide on the new slip plane. However, the time spent by gliding between obstacles is significantly less than the time spent during the climb process and therefore climb controls the rate. Creep occurs at very low strain rates; therefore, it is important to recognise the difference in deformation occurring for loading conditions with significantly higher strain rates such as an initial monotonic tensile load or a cyclic load. To recognise the combination of the two phenomena, a superposition of power laws is used, one that is relatively rate insensitive (associated with dislocation glide and cross slip), and the other rate sensitive (associated with dislocation glide and climb). Similar modifications have also been postulated in previous studies [45, 54-59]. The combination of terms is aimed at providing a means of modelling complex loading conditions which involve a combination of multiple loading conditions and dwell periods. The flow rule was therefore decomposed into two power laws as presented in Eq 11.

$$\dot{\gamma}^{\alpha} = \left[\dot{\gamma}_{0,1}\left(\frac{|\tau^{\alpha} - X^{\alpha}|}{g^{\alpha}}\right)^{n_1} + \dot{\gamma}_{0,2}\left(\frac{|\tau^{\alpha} - X^{\alpha}|}{g^{\alpha}}\right)^{n_2}\right] sgn(\tau^{\alpha} - X^{\alpha}) \tag{11}$$

where $\dot{\gamma}_{0,1}$ and $\dot{\gamma}_{0,2}$ are the reference strain rate for time independent plasticity and time dependent plasticity respectively, while n_1 and n_2 are the strain rate sensitivities for time independent and time dependent plasticity respectively.

The authors recognise that there will also be a grain size dependence on the evolution of the slip hardening represented as g^{α} which the current constitutive model does not consider. Additionally, in the presented constitutive model development, the evolution of g^{α} is the same in both regimes. However, the evolution of g^{α} in the time independent regime has the potential to be evolving differently from the time dependent regime. It is the intention of future work to consider these modifications.

2.3.3 Recovery

The final modification to the flow rule is the addition of a recovery term to the slip hardening equation. The formulation of the recovery term is determined based on the previous theoretical work on competing effects of work hardening and recovery occurring in metals [60, 61], where recovery is associated with dislocation climb and dislocation annihilation [62]. Using the formulation provided in [63], the flow stress of the material (σ_0) is a function of both hardening and recovery, which can be expressed as,

$$\dot{\sigma_0} = h\dot{\varepsilon} - r \tag{12}$$

where h is the hardening and r the recovery. For the application to the constitutive models in this study, the flow stress (σ_0) in Eq 12, is replaced in this case with g^α. This is done to represent the overall slip hardening evolution and therefore dislocation interactions, which follows the approach by Gittus [64] to recognise that the current flow stress is a function of the current dislocation density,

$$\dot{g^\alpha} = h\dot{\gamma^\alpha} - r \tag{13}$$

The hardening component defined by h is incorporated using Eq 7. The recovery component can be derived by applying the following as suggested by Evans, et al. [65],

$$r \propto v g^{\alpha d} \tag{14}$$

where v is the mobility of the climbing dislocation segments, and d is a power to control the influence of the evolution of slip hardening. To incorporate the temperature dependence on the recovery component, thus ensuring the magnitude of recovery is dependent on the temperature, the process outlined in Evans, et al. [65] was used. In this approach the dependence on v is characterised by an activation energy giving the following relationship,

$$r = A g^{\alpha d} \exp\left(-\frac{Q}{RT}\right) \tag{15}$$

where A is a fitting parameter, Q is the activation energy for creep, T is the temperature, and R is the universal gas constant.

Substituting the hardening component in Eq 7 and the recovery component in Eq 15 into Eq 13 gives the following final formulation for hardening and recovery,

$$\dot{g^\alpha} = h_0 \sum_{\beta=1}^{N_s} \left\{ \left(1 + \frac{h_0 \gamma_{sum}}{\tau_0 m}\right)^{m-1} \left|\dot{\gamma}^\beta\right| \right\} - A g^{\alpha d} \exp\left(-\frac{Q}{RT}\right) \tag{16}$$

From Eq 16, the recovery component includes the total value of slip hardening (g^α). This ensures that the recovery processes have greater potential to occur with increased dislocation accumulation.

This formulation of recovery evolves according to g^α which itself is influenced by the accumulation of intragranular residual stress (X^α). However, the current constitutive model in this study does not explicitly include the dynamic recovery of the dislocation structure. If this was included, the dislocation density would be reduced which is analogous to a reduction in g^α. This would lead to a change in the recovery. Therefore, due to the current formulation of the constitutive model, the evolution of thermal recovery is only affected by the intragranular residual stress and not the dynamic recovery of the dislocation structure.

3.Experimental data

3.1 Material

Experimental data was extracted from the work by [32-34] and [9, 12] using 316H stainless steel loaded at 550°C.

3.2 Loading Conditions

Different loading conditions were used in the calibration and validation of the model. These included single strain-dwell and load-dwell loading in addition to a multiple strain dwell loading condition. Details of the different single strain-dwell loading conditions used in the study are listed in Table 1, with a schematic of the type of loading provided in Figure 1. The experimental data used to compare against the simulation results was obtained from [32-34]. The single load dwell used in this study is listed in Table 2, with the simulation results from this dwell compared to experimental data from Wang, et al. [34].

Load-up stress (MPa)	Strain dwell time (hours)
250	1,055
246	25
230	14,310

Table 1 Summary of single dwell stress relaxation tests considered in the study which are schematically demonstrated in Figure 1. The experimental data used to compare with simulations from [32-34].

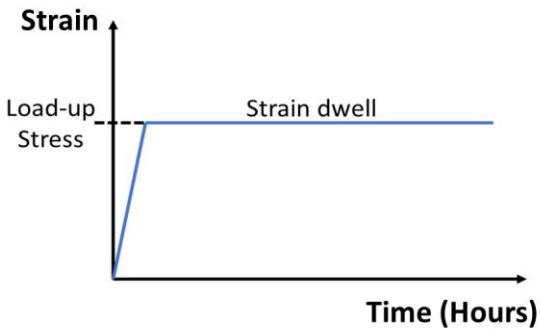

Figure 1 Schematic of the single strain dwell used in calibration and validation simulations.

Load-up stress (MPa)	Load dwell time (hours)
253	25

Table 2 Summary of single dwell load-control creep test. The experimental data used to compare with simulations from [34].

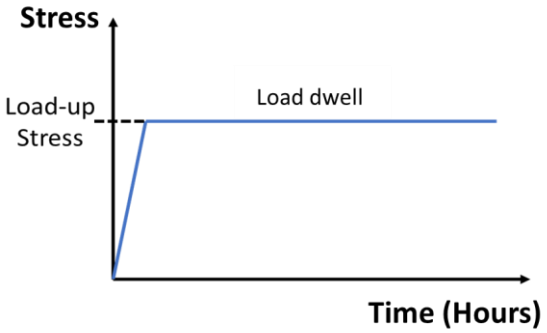

Figure 2 Schematic of the single load dwell used in the validation simulations.

The multiple strain dwell loading condition is schematically demonstrated in Figure 3, with information on the stress loadings and dwell times provided in Table 3. The experimental data used for this investigation was from [9, 12].

Loading sequence	Stress at the start of strain dwell (MPa)	Strain dwell time (sec)
1st load-up	95.0	3303
2nd load-up	155.6	3170
3rd load-up	191.9	4639
4th load-up	209.9	740
5th load-up	257.8	2460
6th load-up	270.7	3430
7th load-up	321.1	3120
8th load-up	364.0	2320

Table 3 Further information on the values of the load-up stresses and strain dwell times used in the multiple dwell loading sequence, as schematically represented in Figure 3. Experimental data sourced from [9, 12].

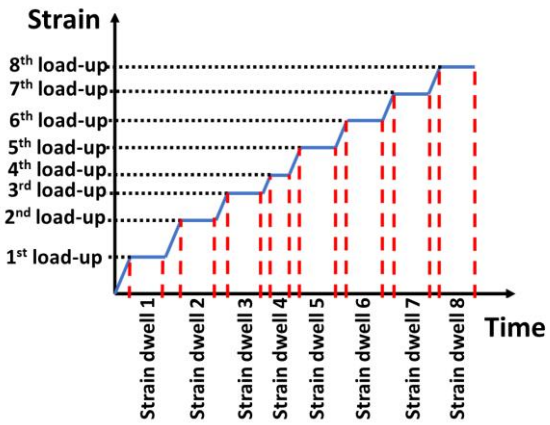

Figure 3 Schematic of the multiple strain dwell loading scenario used in the model validation simulations. Further information on the load-up stresses and time periods used in the strain dwells is provided in Table 3.

4. Finite Element Implementation

In the following sections the details of the approach taken to construct the representative volume is described followed by the details of the of the finite element model. It is also important to outline some of the assumptions made during the construction of the FE model. The dimensions of the model considered is on the meso-scale, which is the scale that lies between the macroscopic and atomistic [66]. Additionally, the approach taken in the development of the FEM does not consider grain boundary sliding which has been found to have a more profound effect for materials with much smaller grains than being modelled in this study [67, 68].

4.1 Representative Volume Construction

The representative volume was built synthetically using DREAM.3D [69] during which a random texture was assigned to the grains within the volume. The final synthetic microstructure is provided in Figure 4, comprising of 226 grains. The number of grains was based on the work by Petkov, et al. [30] who conducted a sensitivity analysis using the same material being modelled in this study and concluded that no significant change in macro-scale predicted results was noticed with RVEs containing greater than 200 grains. Since 316H stainless steel is a face centred cubic (FCC), slip was modelled to occur on 12 systems ($\{111\} < 110 >$).

The RVE was then meshed using 8-node linear brick elements (C3D8), totalling to 32,768 elements.

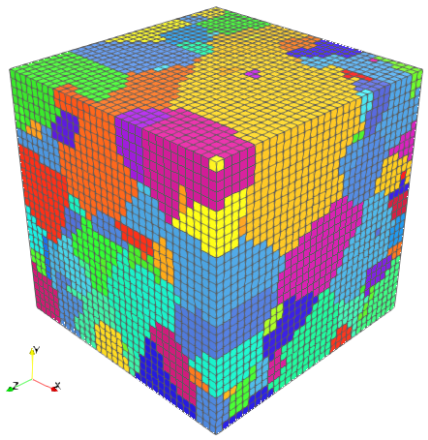

Figure 4 The RVE created using DREAM.3D where the colours represent different grains within the volume.

4.2 Finite Element Analytical Details

The constitutive relations were implemented by modifying a user-defined material subroutine (UMAT) developed originally by Huang [40]. To solve for an increment in slipping rate ($\dot{\gamma}^{\alpha}$) an implicit time integration scheme ($\Delta\gamma^{\alpha} = \Delta t\dot{\gamma}_{t+\Delta t}$) was employed and the Newton-Raphson iterative method to solve the nonlinear equations was used (details of the modification and implementation of this approach is given in Appendix A). The implemented elasto-plastic tangent stiffness matrix used by the finite element solver during the iteration procedure was derived by Huang [40]. All simulations were conducted using the finite element code ABAQUS/Standard [70].

The maximum time increments used in the simulations are listed in Table 4. The tensile load refers to the loading during which an incrementally increasing stress or strain is applied to the model.

Table 4 Time increments used in the different loading conditions used in this study.

Load Case	**Maximum Time Increment(secs)**
Tensile	0.05
Strain Dwell (>10,000 hours)	100,000
Strain Dwell (<1000 hours)	100
Load Dwell (<25 hours)	100

The boundary conditions employed are important in ensuring the RVE deformation is representative of the macro-scale behaviour. This is achieved by assuming symmetry, through the application of the boundary conditions as motivated by [71-74] and demonstrated in Figure 5. The faces of the RVE that are not assigned a boundary condition ($U_i = 0$) can deform freely.

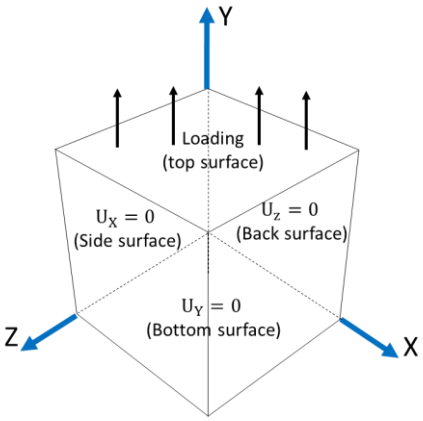

Figure 5 Surface breakdown of the RVE to demonstrate the application of boundary conditions.

To obtain the global stress-strain response of the RVE, an averaging method used by Kashinga, et al. [75] was employed, which uses volume integrals,

$$\overline{\sigma_{ij}} = \frac{1}{V_T}\int \sigma_{ij} dV \quad , \qquad \overline{\varepsilon_{ij}} = \frac{1}{V_T}\int \varepsilon_{ij} dV \tag{17}$$

where $\overline{\sigma_{ij}}$ and $\overline{\varepsilon_{ij}}$ are the average stress and strains respectively, which represents the global response, V_T is the total volume of the RVE, V is the element's volume and σ_{ij} and ε_{ij} are the local stresses and strains. To compute the integral, the local stress, strains and volume were obtained from integration points of each element in ABAQUS. A post-processing Python script was developed and used to access the results from the ABAQUS output file (odb file) to complete the averaging method across all integration points in the model and arrive at a global response.

5. Parameter Calibration

In the following sections the methods used to calibrate the parameters adopted in the constitutive models is presented. The total number of parameters which require calibration against experimental data are eleven ($h_o, \tau_0, m, \dot{\gamma}_{0,1}, \dot{\gamma}_{0,2}, n_1, n_2, d, A, h, h_D$) and six other parameters, constants, and state variables are directly measured ($c_{11}, c_{12}, c_{44}, Q, R, T$). Bounds on the eleven parameters can be determined from examples of their use in previous studies, as well as related experimental findings. This narrows the search for a suitable parameter. As much detail as possible is given to describe each of the processes undertaken to determine these values to provide ease of implementation to anyone endeavouring to use these constitutive models for different materials. Additionally, the approach given makes use of only two data sets for successful calibration of the parameters, allowing for ease of application of the presented model.

5.1 Strain Hardening and Kinematic Hardening Parameters

The slip hardening parameters were calibrated by fitting to tensile stress-strain experimental data obtained from experiments using 316H stainless steel at 550°C by [9, 12]. The value of h_0 was optimised to fit the stress-strain evolution beyond yield, while also considering the influence of the component of kinematic hardening. Since τ_o influences the initiation of slip, this value was

altered to provide an accurate initial macro-scale yield strength. Finally, m was calibrated to provide improved fit to predicted stress at large strains.

To provide an initial estimate of the parameters which control the evolution of kinematic hardening, a calibration process was utilised. Using experimental data from [6], the first cycle from symmetric strain-controlled tests at a strain range of $\pm 0.6\%$ with R=-1 were extracted and the total intergranular and intragranular stress were calculated using Cottrell's method [76] to estimate the total back-stress. The total kinematic (X) and isotropic hardening (R) were estimated using Cottrell's method by probing different locations on the hysteresis loop as demonstrated in Figure 6 where σ_{eff} is the effective stress which is a combination of the yield stress (σ_y) and the isotropic hardening ($\sigma_{eff} = R + \sigma_y$).

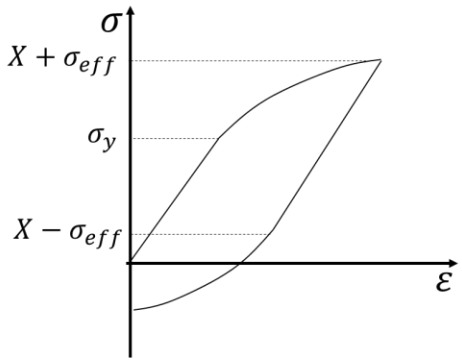

Figure 6 A schematic demonstrating Cottrell's method [76] to provide an estimate to the magnitude of kinematic hardening (X), which was then used to estimate the parameters which control the magnitude of intragranular residual stress.

Applying this approach leads to a total back-stress of 118MPa, which provides an upper bound on the saturated value of intragranular residual stress evolving according to Eq. 10 . Starting with this value, monotonic simulations could be undertaken and compared to the experimental stress-strain evolution. Since this value is the combination of both intergranular and intragranular stresses, the values of h and h_D in Eq. 10 were then optimised to reduce the magnitude of the ratio h/h_D to incorporate the intergranular residual stresses inherent to the CPFE. From Figure 7 it is apparent that the final parameters provide a good fit to the experimental tensile stress-strain data.

It is important to note that this calibration process for h and h_D is constrained to the simulation of a limited number of cycles (approximately less than 5 cycles). If the model is to be used in the simulation of loading conditions containing a large number of cycles (possibly leading to saturation of the hysteresis loops), the calibration procedure for h and h_D would have to also include this type of loading condition. Doing so would allow for slight adjustments of the values of h and h_D to prevent early saturation of the hysteresis loops.

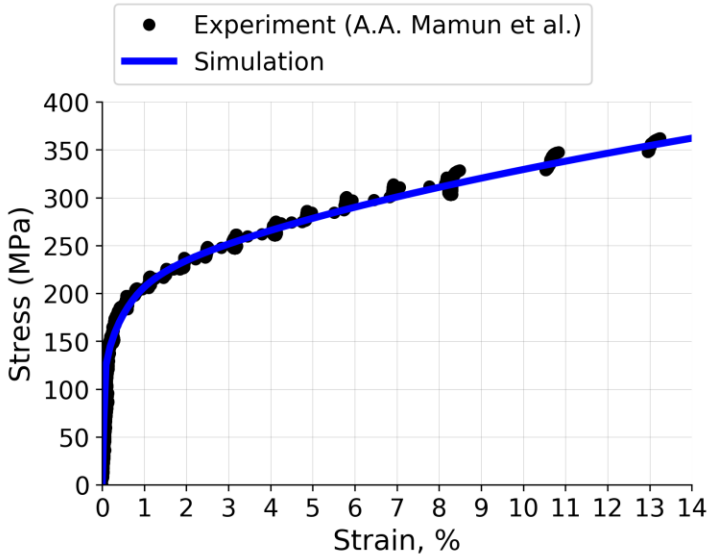

Figure 7 Stress-strain evolution of 316H at 550°C from low to high strain under tensile loading.

5.2 Slip Rate Parameters

The first power law in Eq 11 is used to model the dominant monotonic/cyclic loading, therefore, the parameters were calibrated using monotonic tensile data. Since n_1 controls the rate sensitivity, a large value was selected to ensure slip associated with this power law occurred predominantly during monotonic/cyclic loads and did not transfer across into the time dependent regime where the second power law in Eq 11 is dominant. Selection of the size of n_1 was also done to ensure that there were no issues with convergence (which has been shown to be a problem by Harewood, et al. [77]).

To develop the values of $\dot{\gamma}_{0,2}$ and n_2 a calibration strategy used in [58, 59] was employed which used creep experimental data to calibrate the parameters. In this study, the experimental data used was strain dwell experimental results from [32, 33] at 230MPa at a temperature of 550°C with focus on the early stage of slip evolution (<200 hours). To improve the efficiency of the calibration process, values for $\dot{\gamma}_{0,2}$ and n_2 were selected based on information from previous studies. From a previous study [58] implementing a similar combination of power-laws, the value of n_2 was selected to be 9. Therefore, the value for n_2 in this study was expected to be in the vicinity of this value. Additionally, since slower slip rates are associated with this power law, a small value for $\dot{\gamma}_{0,2}$ was required, which was also noticed in [58] where a value as small as $1.57 \times 10^{-9} s^{-1}$ was implemented. Therefore, values of this approximate size were expected in the calibration process. Following this process, the optimised values for $\dot{\gamma}_{0,2}$ and n_2 provide a good fit to the experimental data, with the results given in Figure 8.

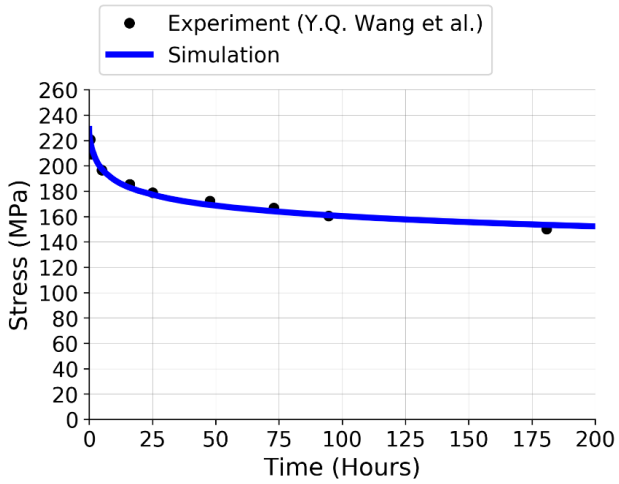

Figure 8 The final calibrated fit to the early stages of the stress relaxation using data gathered from [32, 33]. This calibration is used to arrive at the correct values for $\dot{\gamma}_{0,2}$ and n_2.

5.3 Recovery Parameters

The parameters defining the recovery process were calibrated from experimental data from long (>1000 hours) load or strain dwell tests during which the recovery is more dominant. Firstly, the activation energy was taken as the average across the expected stress range as given by Kloc, et al. [78]. The value of d in Eq 16 could firstly be estimated from the understanding that for intermediate/high stress and temperatures from ~ 0.4 to $0.7T_m$ its value should be approximately 3 or greater [65]. Therefore, using the value of 3 as a starting point, the values of d and A could be adjusted to ensure the recovery evolves effectively enough to provide a good fit to long dwells (simulating the stress relaxation beyond approximately 1000 hours). In this work, a strain dwell was used as the calibration data, by once again using the experimental data with a maximum stress of 230MPa at a temperature of 550°C gathered by [32, 33]. d and A were then adjusted to provide a good fit to this data beyond approximately 1000 hours with the final fit provided in Figure 9.

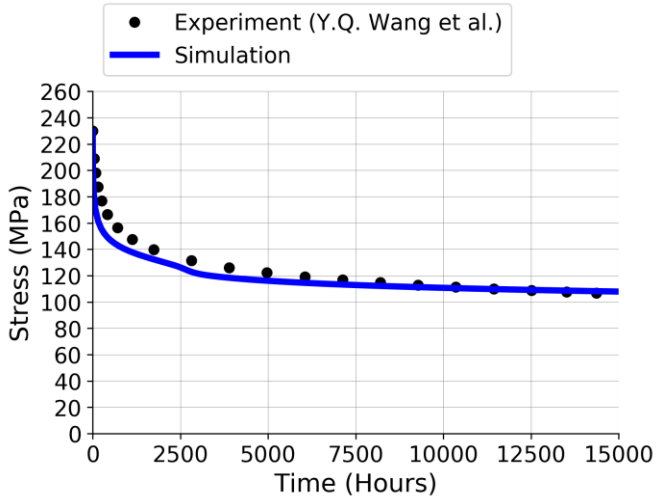

Figure 9 The final calibrated fit to the later stages (>1000 hours) of stress relaxation using data gathered from [32, 33].

The final and complete set of parameters, constants, and state variables used in simulations are listed in Table 5 (with the following parameters derived in this work: $h_o, \tau_0, m, \dot{\gamma}_{0,1}, \dot{\gamma}_{0,2}, n_1, n_2, d, A, h, h_D$).

Table 5 Final material parameters, constants, and state variables used in simulations.

Equation	Parameters	Value
Elastic modulus	c_{11}, c_{12}, c_{44}	183.9 GPa, 123.4GPa, 91.5GPa
Slip hardening	h_o, τ_0, m	500MPa, 45MPa, 0.35
Slip rate	$\dot{\gamma}_{0,1}, \dot{\gamma}_{0,2}, n_1, n_2$	$1s^{-1}$, $3\times 10^{-8}s^{-1}$, 500, 10
Recovery	Q, R, T, d, A	418KJ/mol, 8.31J/mol K, 823K, 3, 3×10^{16}
Intragranular stress	h, h_D	6555MPa, 245

6. Macro-Scale and Meso-Scale Prediction Results

In the following sections the macro-scale and meso-scale simulations are presented for several different loading conditions. The accuracy of the predictions are quantified using an error calculation scheme based on the discrete Fréchet distance algorithm developed by Eiter, et al. [79]. The algorithm uses the nodes of the polygonal curves to provide a measure of the similarity between the curves, which is based on the original work by French mathematician Fréchet [80]. It has the additional benefit of the two polygonal curves not requiring the same number of points, which is of particular advantage in the comparison of the experimental and predicted data in this study. To allow for effective comparison of the Fréchet distances calculated for different magnitudes of stress and strain, the experimental and predicted points were individually

normalised using the maximum value in each set of experimental data. This ensured the Fréchet distance would range between 0 and 1.

6.1 Macro-Scale Prediction/Validation

The model prediction is compared with the experimental results for loading containing multiple strain dwells in Figure 10. From the results, it is evident that the model in combination with the parameter calibration procedure produces very accurate simulation results, with the curve similarity calculated to be 97%. The last dwell is the least accurate, with the model over-predicting the initial rate of relaxation. This results in an initial fast drop in stress at the start of that dwell, which causes the over-prediction in relaxed stress. This highlights a possible issue with the model at predicting the evolution of stress at high strains (>14% strain), which could be the consequence of additional mechanisms occurring in the material the proposed model does not consider in full. This will require further investigation in planned future studies.

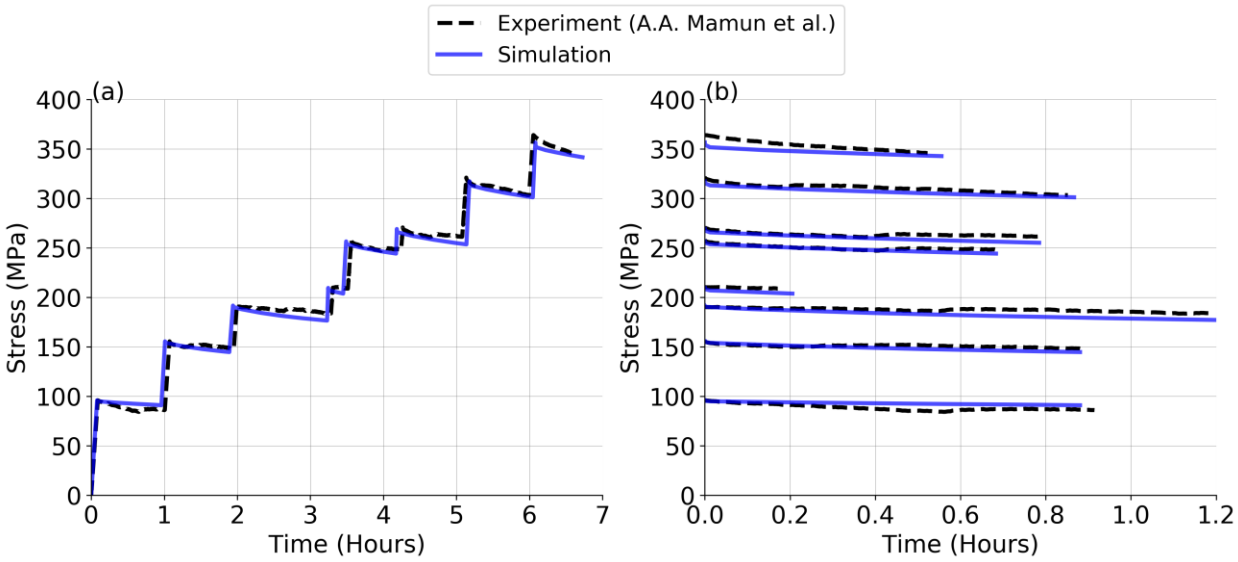

Figure 10 Simulation results achieved for the multiple strain dwell loading case where (a) shows the complete loading history and (b) displays the results for each individual dwell to provide further clarity of the achieved simulation accuracy.

To consider the influence of the recovery component of the slip hardening and to further validate the model, another single strain dwell loading case was considered. The results of the simulation compared to experimental data is provided in Figure 11, which shows the simulation once again being in good agreement with the experimental results. The relaxation rate during the early stages (<100 hours) (Figure 11 (a)) of the dwell is very well simulated, which suggests that the model's evolving shear strain when averaged across all the grains within the RVE is progressing at a rate representative of that occurring during the dwell. Additionally, the gradual saturation of the evolving strain at the later stages of the dwell (>500 hours) (Figure 11 (b)) is also well captured by the model (92% curve similarity) which indicates that the recovery component of the slip hardening formulation is activating correctly to ensure the saturation of the shear strain is

also representative of that occurring in the material. This provides further support to the importance of the modifications made to the constitutive models.

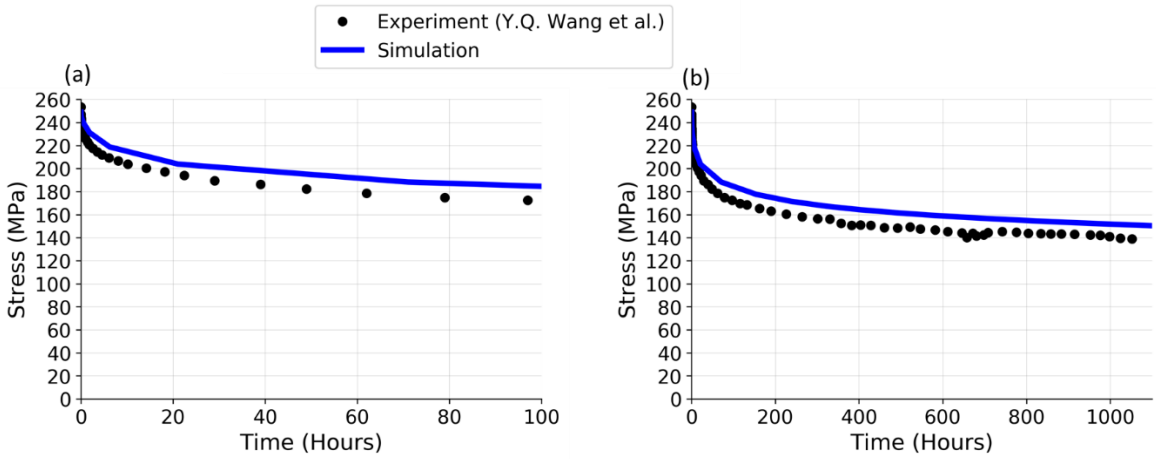

Figure 11 Comparison of the simulated response of the stress relaxation during a single strain dwell compared to the experimental data from [32, 33].

6.2 Meso-scale prediction/validation

With the developed constitutive models giving accurate macro-scale results, meso-scale information was then interrogated to make full use of the CPFE. This level of interrogation compliments experimental findings, since it provides an opportunity to investigate grains and their environment and how these contribute to the development of localised stress and plastic strain. One area of interest the CPFE could provide deeper insight into is the creep inhomogeneity reported to occur during creep by [9, 11]. Similar to plastic anisotropy during load-up, creep inhomogeneity is a phenomenon also associated with grain-to-grain interactions, but instead refers to grain-to-grain interactions occurring due to different creep rates between grains [9, 12]. Additionally, creep inhomogeneity is influenced by prior plastic loading since different levels of plastic deformation occurring between grain families during initial loading has potential to also influence the heterogeneity of creep strain accumulation in the grain families during subsequent creep [9, 12].

The plastic anisotropy can be visualised by calculating the ideal elastic lattice strains during load-up and determining whether the lattice strains are deviating from these ideal elastic values. The ideal elastic strains are calculated using the macro-scale stress relaxation and the diffraction elastic constants determined by Wang, et al. [34] in conjunction with the following relationship,

$$\varepsilon_{hkl} = \frac{\sigma}{E_{hkl}} \tag{18}$$

where ε_{hkl} is the ideal elastic strain for the [26] grain family, E_{hkl} is the elastic modulus for each grain family, and σ is the macro-scale stress.

Neutron diffraction experiments were undertaken by Wang, et al. [34], who investigated the lattice strain evolution in both strain- and load-control dwells. The developed CPFE was used to simulate the lattice strain evolution during a strain dwell and load dwell to demonstrate whether

the model could effectively distinguish between the difference in evolution of lattice strain. The details of the loading investigated involved a strain dwell during which an initial loading up in tension to a stress of 246MPa was undertaken followed by a strain dwell for a period of approximately 25 hours, as summarised in Table 1. For the load dwell loading case, an initial loading up in tension to a stress of 253MPa was applied followed by a dwell for approximately 25 hours, as summarised in Table 2.

To compare simulated lattice strain against the experimental values, the process used to extract the lattice strains for each family from the CPFE model required determining which grains within the RVE have {*hkl*} planes orientated to contribute to diffraction. To do this, the normal vector to the {*hkl*} planes in the local lattice coordinate system was calculated as follows,

$$\boldsymbol{N}_{hkl} = \frac{(h\boldsymbol{e}_1 + k\boldsymbol{e}_2 + l\boldsymbol{e}_3)}{\sqrt{h^2 + k^2 + l^2}} \tag{19}$$

where $\boldsymbol{e}_1$, $\boldsymbol{e}_2$, $\boldsymbol{e}_3$ are the orthogonal vectors of the local lattice configuration.

The normal of the plane in the global coordinate system ($\boldsymbol{n}_{hkl}$) was then obtained by rotating the normal in the local lattice configuration ($\boldsymbol{N}_{hkl}$) using the rotation matrix ($\boldsymbol{R}$) based on the Euler orientation angles (φ_1, Φ, φ_2) describing the orientation of the grain. The rotation matrix is formed by combining three successive rotations based on the convention of Bunge, where the rotations are first around the Z axis, then X axis, and finally around the new Z axis. This results in the following matrix,

$$\boldsymbol{R} = \begin{bmatrix} \cos\varphi_1 \cos\varphi_2 - \cos\Phi \sin\varphi_1 \sin\varphi_2 & \sin\varphi_1 \cos\varphi_2 + \cos\Phi \cos\varphi_1 \sin\varphi_2 & \sin\Phi \sin\varphi_2 \\ -\cos\varphi_1 \sin\varphi_2 - \cos\Phi \sin\varphi_1 \cos\varphi_2 & \cos\Phi \cos\varphi_1 \cos\varphi_2 - \sin\varphi_1 \sin\varphi_2 & \sin\Phi \cos\varphi_2 \\ \sin\Phi \sin\varphi_1 & -\sin\Phi \cos\varphi_1 & \cos\Phi \end{bmatrix} \tag{20}$$

The normal in the global coordinate system was then calculated using the following relationship,

$$\boldsymbol{n}_{hkl} = \boldsymbol{R}^T \boldsymbol{N}_{hkl} \tag{21}$$

The angle between the diffraction vector ($\boldsymbol{g}$) and the plane normal defined in the global coordinate system ($\boldsymbol{n}_{hkl}$) was then calculated using the following,

$$\theta = \cos^{-1} \frac{(\boldsymbol{n}_{hkl} \cdot \boldsymbol{g})}{(|\boldsymbol{n}_{hkl}| \cdot |\boldsymbol{g}|)} \tag{22}$$

The grain from which the lattice strains were extracted was chosen if the calculated angle between the two vectors (θ) was within a specified tolerance of $\pm 7.5°$ to be consistent with the process used for extracting the experimental data, in addition to ensuring enough grains were averaged across.

The average lattice strain across each individual grain with $\{hkl\}$ planes oriented within the tolerance specified was calculated using the following formulation,

$$\overline{\varepsilon_{ij}} = \frac{1}{V_T} \int \varepsilon_{ij} dV \tag{23}$$

where $\overline{\varepsilon_{ij}}$ are the average lattice strain across the grain, V_T is the total volume of the grain, V is the element's volume and ε_{ij} is the element lattice strain.

The lattice strain evolution of the grain family was then calculated by taking the average response across all identified grains within the $\pm 7.5°$ tolerance according to the following equation,

$$\varepsilon_{hkl} = \frac{\sum_{N=1}^{N_{grain}} \overline{\varepsilon_{ij}}}{N_{grain}} \tag{24}$$

where ε_{hkl} is the lattice strain for the $\{hkl\}$ planes, and N_{grain} is the number of grains identified to be within the $\pm 7.5°$ tolerance.

Firstly, the macro-scale tensile stress-strain evolution between the experimental results reported by Wang, et al. [34] and the those simulated by the model were compared to ensure the modelling capability could accurately predict the macro-scale results. This was a necessary step to validate the overall accuracy of the model before extracting information on the meso-scale. The simulation and experimental tensile results are compared in Figure 12, with the results being in good agreement, with an 83% curve similarity, validating the use of the developed CPFE model to investigate grain-level deformation.

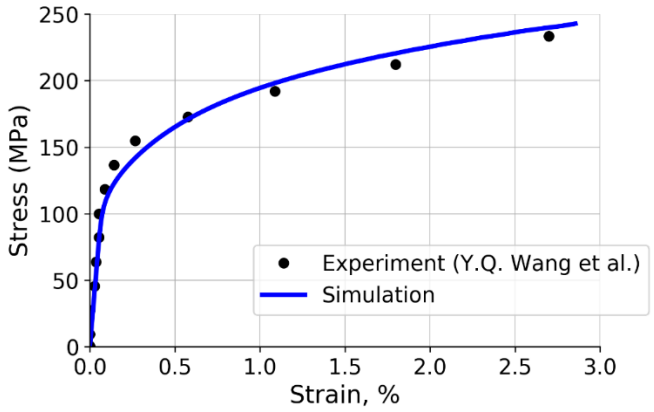

Figure 12 Comparison of the simulated and experimental tensile results from [34] for 316H stainless steel at 550°C

Applying the method outlined to extract grain average responses for each grain family from the CPFE, the lattice strains for the {111}, {200}, {311}, and {220} families in the longitudinal direction during load-up were extracted and compared to the lattice strain evolution experimentally determined by Wang, et al. [34]. The comparisons are made in Figure 13.

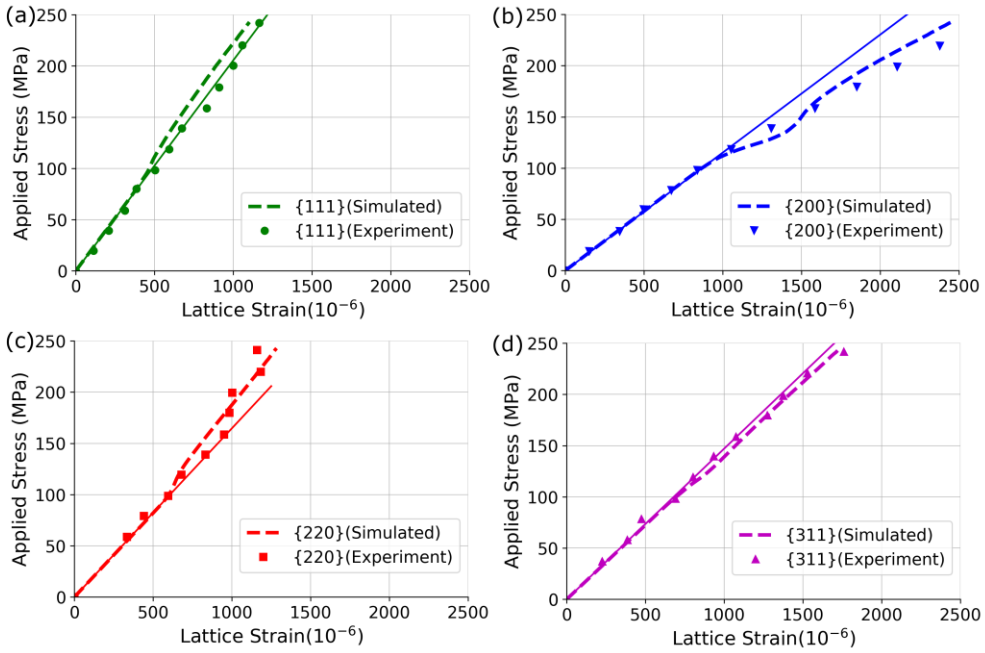

Figure 13 Experimental longitudinal lattice strain evolution from [34] for grain families (a) {111}, (b) {200}, (c) {220}, and (d) {311} compared to simulated lattice strain evolution.

The simulation results for the grain families compare well with the extracted experimental results from Wang, et al. [34]. In addition to the lattice strain evolution, the ideal elastic line (using Eq 18) was also added to each figure to demonstrate the deviation of the lattice strain from elastic conditions, therefore, highlighting the relative amount of intergranular strain within grain families. The ability of the model to predict the intergranular strain evolution during plasticity is therefore confirmed by the results with the lattice strain evolution within the grain families showing comparatively similar behaviour to that seen in the experimental data. Calculating the similarity of curves for each grain family, the percentage of similarity for grain families {111}, {200}, {220}, {311} is given as 90%, 91%, 82%, and 90% respectively, which provides an indication of the overall accuracy of the simulation. Visually, it is evident that the simulation results for grain families {220} and {200} show deviation from the ideal elastic line which follows the same trend as that seen experimentally. During the initial loading stage, each grain family behaves elastically until approximately 110MPa where in the experimental and simulation data there is a deviation from the ideal elastic line for the {200} and {220} grain families in opposite directions. This is indicative of strong plasticity effects in these grain families. The simulation shows the same trend as that seen experimentally where in the {220} grain family, plastic deformation is occurring, which is observed by the decrease in elastic strain progression with increasing applied stress. This results in an increase in elastic strain in the {200} grain family, which is observed by the non-linear deviation in the opposite direction to that occurring in the {220} grain family.

The next step was to consider the strain dwell, with Figure 14 comparing the simulation of the macro-scale stress relaxation with the experimental findings from Wang, et al. [34]. The simulated results were calculated to provide 94% curve similarity with the experimental findings, which provides indication of the accuracy of the macro-scale simulations for this strain dwell test.

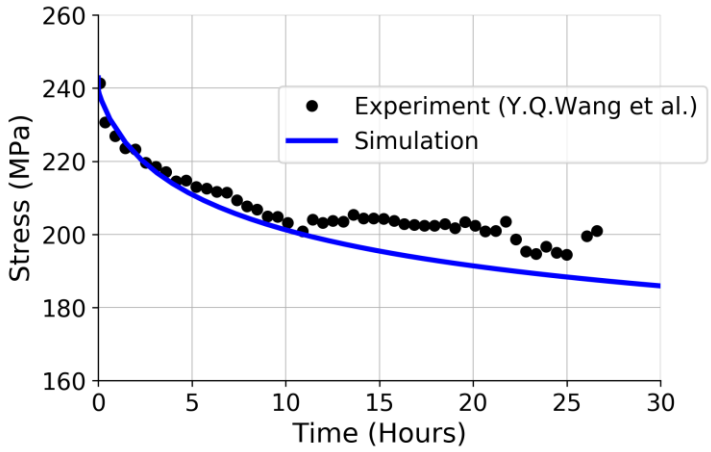

Figure 14 Comparison of the macro-scale simulated and experimental stress relaxation during the strain dwell from [34] for 316H stainless steel at 550°C.

The relaxation in lattice strains occurring during the dwell for each grain family were then extracted and compared to the experimental results in Figure 15. In Figure 15, the strains for each grain family were normalised with respect to the maximum strain within each grain family. Doing so ensures the lattice strain evolution for each grain family starts from zero, allowing for ease of comparison in evolution. Also included in the figure is a line of best fit to provide a better visual representation of the trend of the experimental data. The simulated lattice strains are comparable with the experimental results, with curve similarity calculated as the following percentages 72%, 60%, 86%, and 65% for grain families {111}, {200}, {220}, and {311} respectively. The magnitude in relaxations between grain families show the same trend as that in the experimental case, where the magnitude of relaxation greatest in the {200} grain family and the least in the {111} grain family.

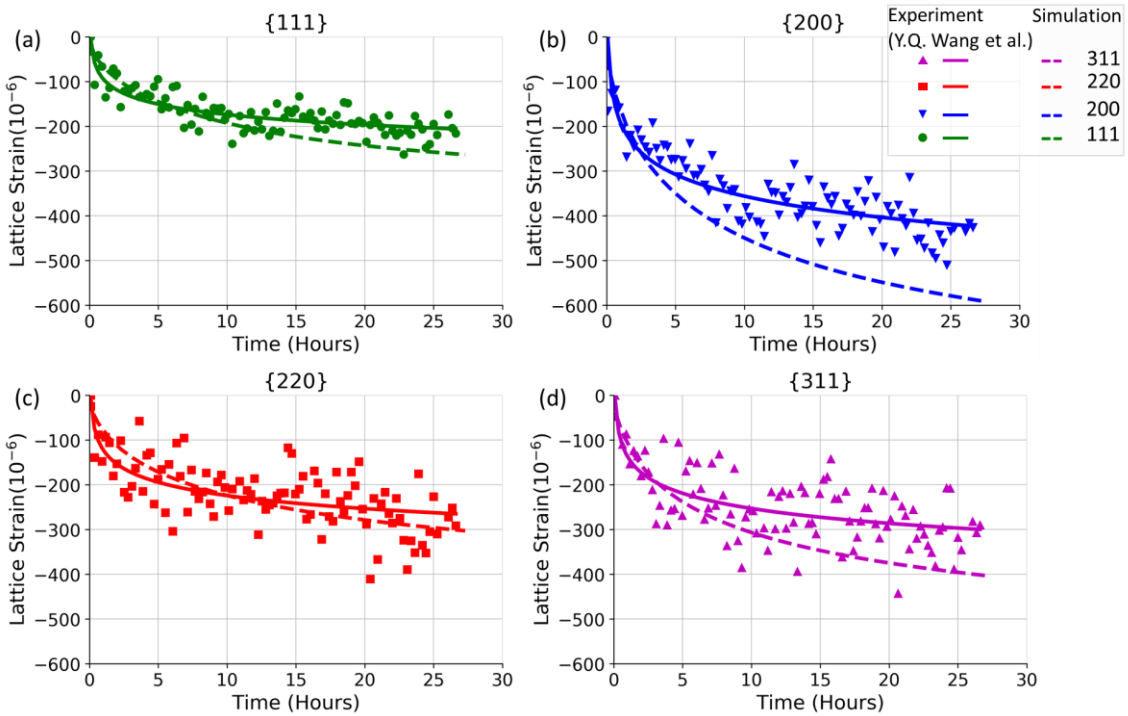

Figure 15 Experimental and simulation comparison of the relaxation of lattice strain for each grain family (a) {111} (b) {200} (c){220} (d) {311}.

The most accurate predicted results are the relaxation in lattice strains for grain families {111} and {220}, where the calculated curve similarities are 72% and 86% respectively. The least accurate predictions are for the {200} and {311} grain families, where the curve similarities are 60% and 65% respectively. The inaccuracy occurs in predicted lattice strain relaxation in grain families {200} and {311} outside of the 5-hour window of the dwell, where the simulation overpredicts the magnitude of lattice strain relaxation.

In addition to the strain-controlled dwells, the simulation of the macro- and meso-scale behaviour during a load-control dwell was also investigated. Figure 16 compares the macro-scale simulation results for the load dwell with the experimental findings from Wang, et al. [34]. The model underpredicts the creep strain accumulated during the dwell, with the curve similarity measured to be 64%. This identifies a potential issue with the model's capability to accurately simulate the creep strain during a load-control dwell with the parameters calibrated using strain-control experimental data.

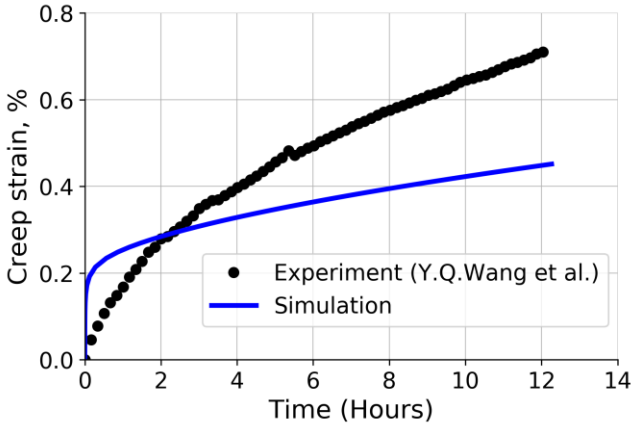

Figure 16 Comparison of the macro-scale simulated and experimental creep strain during the load dwell from [34] for 316H stainless steel at 550°C.

To also investigate the evolution of the lattice strains during the load dwell, the lattice strains for each grain family in the longitudinal direction were compared to the experimental results in Figure 17. From the experimental results, it is evident that the lattice strain during the dwell remains predominantly constant, which is also observed in the simulation results. The evolution of intergranular strain is different to that occurring during the strain-controlled dwell where the lattice strains are observed to relax. This is an important finding as it confirms the model's ability to recognise the difference in grain-to-grain interactions during the two different controls.

The overall magnitude of the lattice strains for each grain family corresponds to the intergranular strain reached during the initial load-up to 253MPa. Therefore, the difference observed in the simulation for each grain family is indicative of the predicted intergranular strain at 253MPa. The similarity in simulation and experimental results for each grain family {111}, {200}, {220}, and {311} are 90%, 83%, 85%, and 85% respectively.

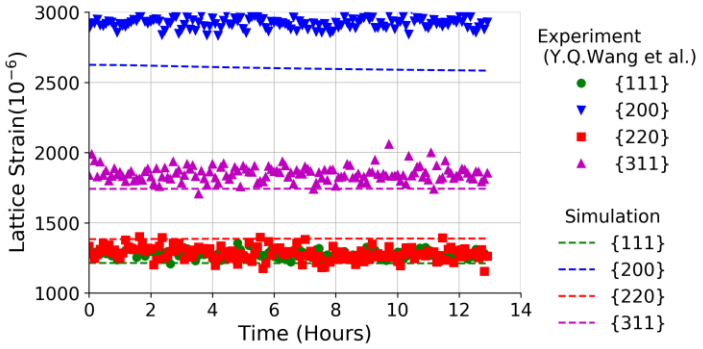

Figure 17 Simulated and experimental lattice strain evolution during the load-control dwell.

Since the lattice strains during the dwell are relatively constant, the contribution to macro-scale creep strain is through the accumulation of plastic strain within grains. Consequently, the

inaccuracy associated with the macro-scale simulation is due to an underprediction in the plastic strain within grains. The reason for this underprediction will be investigated in future work.

7. Discussion

7.1 Macro-scale simulations

The simulation results achieved during the macro-scale validation indicates that separating the shear strain evolution between the time-independent and time-dependent plasticity regimes to recognise the differences in evolution is successful at achieving the desired effect under strain-controlled dwells. The results indicate a significant level of accuracy with success in simulating several different loading conditions. Furthermore, the seamless transition from time-independent and time-dependent regimes during the multiple dwells in Figure 10 further supports the approach to use a superposition of power laws. As demonstrated in previous studies evaluating the influence of prior loading on stress relaxation [81, 82], the magnitude of stress relaxation is influenced by the prior loading history. Therefore, it is expected that the magnitudes of relaxation in the multiple dwell loading case would be indicative of this. The model successfully recognised the prior deformation during the load-ups (due to the time-independent power law) which then influenced the predicted relaxation of stress during the dwell (time-dependent power law). Consequently, the combined influence of the two power laws works effectively not only for a single load case but for more complex loading conditions where the prior deformation history would have an influence on future loading. This is a particularly important finding since it encourages the application of the presented constitutive model to further complex loading where accurate transitioning of deformation from the plasticity and creep regimes is required.

An initial investigation into the predictive capability of the model during a load-control dwell has shown satisfactory preliminary results on the macro-scale. However, this will have to be investigated further through the simulation of multiple loading conditions. It is important a detailed investigation is undertaken to understand the contribution of the evolving shear strain when subjected to different loading conditions. Such an investigation would enhance the understanding of the interaction of the recovery component of the constitutive model on the evolution of shear strain, and therefore the magnitude of predicted creep strain. This will form part of an ongoing study on extending the robustness of the developed modelling capability.

7.2 Meso-scale simulations

The accuracy of the proposed constitutive model is further supported by the meso-scale simulation predictions. Predicted lattice strain evolution during the initial load-up for all three grain families are in very good agreement with the experimental data. Plastic anisotropy is very well simulated with deviation from the ideal elastic lines for each family indicative of the behaviour noticed experimentally. This is especially evident in the {200} grain family which shows the greatest amount of plastic anisotropy, with the predictions displaying a similar magnitude.

The ability of the model to simulate the lattice strain evolution during dwells was also investigated for each grain family. During the strain dwell, the simulation predicted an accurate magnitude of relaxation in the {111} and {220} grain families (72% and 86% curve similarity

respectively). A deviation in the predicted magnitudes of lattice strain from experimental results were noticed in the {200} and {311} grain families, which had the lowest level of curve similarity of the grain families (60% and 65% respectively). This was due to an overprediction in lattice strain in these grain families, particularly evident in the relaxation occurring after the initial 5 hours of the dwell.

Although the reason for this discrepancy is expected to be associated with the model's inability to accurately recognise the grain environment effects (grain-to-grain interactions), the underlying fundamentals contributing to this will require further investigation as part of an ongoing study. One possible direction could be in the investigation of the influence of an initial residual stress state that could exist in the material. Using simulations of different levels of preloading, Hu, et al. [13] demonstrated how this could lead to slight differences in lattice strain evolution, particularly in the {200} grain family. The initial residual stress in the material will change the axial internal strains for each grain family (noticed in neutron experiments conducted by Chen, et al. [83]) altering the internal misfit stresses within the material. This could lead to slightly different lattice strain evolution not only in the initial load up but also during the dwell. Future investigations will be aimed at better quantifying the influence of residual stresses in the material, particularly in the dwell where the largest discrepancy between experimental and predicted results is occurring.

During the load-control dwell, a relatively constant lattice strain evolution for each grain family was predicted. This was supported by the experimental findings by Wang, et al. [34] but has also been observed in additional previous studies [11, 84]. However, interestingly in the study by Chen, et al. [27] using the same material and testing conditions, it was found that intergranular residual strains within the material were affected by a 180 hour creep preloading. This is contradictory to the experimental work of [11, 34, 84] and also the simulation findings as part of this study. Since the intergranular strains during the load-control dwells remained relatively constant, a creep prestrain should have very limited influence on the intergranular strains with the material. However, what this does provide is an interesting future study as to why this discrepancy in experimental findings exists. This could be through the investigation of the influence of thermal strains on inducing internal stresses that affect the elasto-plastic evolution during the initial load up. The magnitude of thermal strains could change between samples which could lead to slightly different lattice strain evolution during the initial load-up. This could be implemented by applying a quasi-thermal expansion eigenstrain developed by Musinski, et al. [85] and subsequently implemented by Pokharel, et al. [86] who showed accurate lattice strain evolution during post-processing heat treatment.

Although this investigation does provide insight into simulation capability of the lattice strain evolution during a load-control dwell, it does not provide a rigorous test of the accuracy since the lattice strains remain relatively unchanged. One approach to investigate the modelling capability further is to interrogate the model's ability to recognise the influence of plastic strain inducing reverse loading on creep, which has recently been investigated experimentally by Al Mamun, et al. [84]. In this study, time dependent changes in lattice strain were observed in grain

families during load dwells following reverse plastic loading. Simulating this type of loading would provide enhanced insight into whether the model could effectively consider the influence of tensile and compressive residual strains from previous loadings. This would be observed as a change from constant to time dependent evolution of lattice strains during the load dwell.

7.3 Future model improvements

7.3.1 Constitutive model parameters

One deficiency in the constitutive model applied is the 11 parameters which require calibration. Bounds on expected values were provided for three of these parameters (n_2,$\dot{\gamma}_{0,2}$, d) to aid in the calibration process of the constitutive models. However, further improvements could be made by adopting a sensitivity analysis such as that applied in [87, 88]. Application of a sensitivity analysis would assist in highlighting key parameters, such as those most influential to simulation accuracy on both the macro- and meso-scales. Additionally, during this process, bounds on expected parameter values would also be determined to further support the calibration process.

7.3.2 Latent hardening

The constitutive model currently considers hardening through accumulated slip (γ_{sum}) in the evolution of g^{α}, to recognise the influence on hardening based on slip in other slip systems. However, the current formulation does not explicitly consider latent hardening (hardening due to active slip systems on inactive slip systems) through the application of a hardening matrix. Future investigations are planned to consider the influence of latent hardening on the meso-scale predictions. Past investigations by Li, et al. [25] showed that during monotonic tensile loading, the extent of latent hardening introduced in the model could have an impact on the simulation of evolving plasticity in grain families. The common phenomenological modelling approach to include latent hardening is based on the experimental findings summarised by Kocks [89] who found that the average ratio of latent hardening rates to self hardening rates is close to 1 for coplanar slip systems and between 1 and 1.4 on noncoplanar systems [44]. This leads to the hardening moduli having the following formulation,

$$h^{\alpha\beta} = q^{\alpha\beta} h^{\beta} \tag{25}$$

where h^{β} is the single slip hardening rate, and $q^{\alpha\beta}$ is the matrix which describes the latent hardening,

$$q^{\alpha\beta} = \begin{bmatrix} \boldsymbol{A} & q\boldsymbol{A} & q\boldsymbol{A} & q\boldsymbol{A} \\ q\boldsymbol{A} & \boldsymbol{A} & q\boldsymbol{A} & q\boldsymbol{A} \\ q\boldsymbol{A} & q\boldsymbol{A} & \boldsymbol{A} & q\boldsymbol{A} \\ q\boldsymbol{A} & q\boldsymbol{A} & q\boldsymbol{A} & \boldsymbol{A} \end{bmatrix} \tag{26}$$

where q is the ratio of latent hardening rate to self hardening rate (ranging from 1 to 1.4), and $\boldsymbol{A}$ is a 3×3 matrix populated by ones.

Based on the findings reported by Li, et al. [25], future extensions of this work will aim to develop deeper insight into the value of q using X-ray or neutron diffraction experimental data. This combined with further insight gained from dislocation dynamics simulations, could be used to

produce a more representative interaction matrix ($q^{\alpha\beta}$), and enhance the simulation accuracy of the model.

7.3.3 Solute and precipitation hardening

The formulation of the applied constitutive model addresses hardening based on the interactions of dislocations with other dislocations. However, there are other possible sources of dislocation interactions on a slip plane in austenitic stainless steels not considered in the formulation of the constitutive model. These include interactions of dislocations with solute atoms and intragranular precipitates. Hu, et al. [13, 46, 90] modified the formulation of the critical resolved shear stress to include these sources of hardening based on a similar formulation applied by Dong, et al. [91]. This constitutive model was used in simulations involving a very similar material as that investigated in this study, which highlights its validity in application in future work.

7.4 Effect of intragranular stresses in the load-up and hold periods

To develop a better understanding on the influence of the intragranular stress development during the load-up and dwell in the strain dwell loading case used in Figures 14 and 15, the intragranular stress in each grain for each slip system were extracted and average across each grain family. The top two most active slip systems where the highest magnitude of intragranular stress developed are provided in Figure 18 to make it more visually comprehensible. As expected, due to the difference in shear strains in the two regimes, the magnitude of intragranular stresses during the load-up are significantly larger than those accumulating during the dwell. Additionally, the overall magnitude of intragranular stresses are significantly smaller than the macro-scale stresses, which was also observed in a similar approach of investigation by Wang, et al. [92].

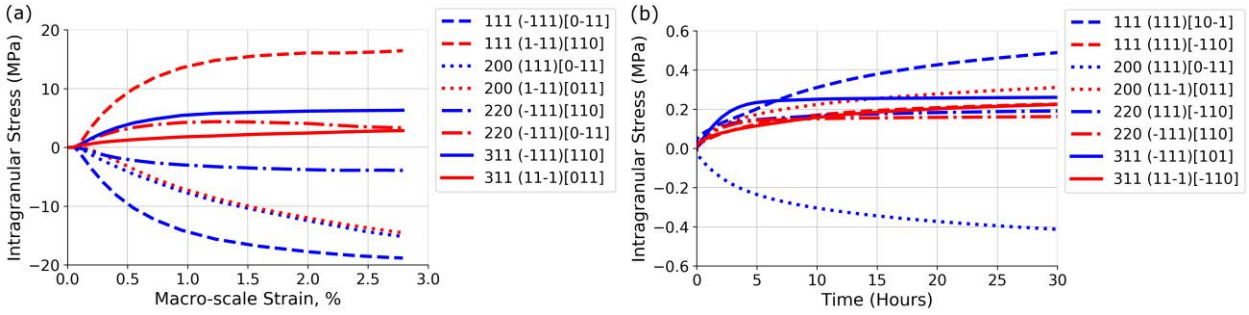

Figure 18 Intragranular stress development for each grain family for the two most active slip systems. The evolution during the load-up (a) and the strain dwell (b) using the loading condition from [34] (load-up to 243MPa and strain dwell)

What is observed from this analysis is the two slip systems which generate the most intragranular stress during load-up and the dwell are different in all grain families except for one case in the {200} grain family. What this suggests is the preferential development of intragranular stress changes between the two loading regimes. Consequently, the influence of the grain environment on the grains of each grain family changes between the load-up and dwell. To improve the understanding on the influence of the evolving intragranular stresses on the grain environment, the change in slip activity between grain families were investigated during the load-up phase and strain dwell with the intragranular stress removed. This required removing the contribution of

intragranular stress on the evolving shear strain in Eq 11 (setting h and h_D parameters to zero). Removing the contribution of the intragranular stress required a change of the h_0 parameter to recognise the required additional amount of hardening and greater contribution of g^{α}. The value of h_0 was therefore changed to 1450MPa to ensure comparable stress-strain predictions as the model with intragranular stress.

Figure 19 compares the evolution of shear strain in all twelve slip system averaged across the grains within each grain family. The shear strain evolution in only the strain dwell is provided to make the figure more visually comprehensible. The influence of the intragranular stress on the activity of slip systems is evident in all four grain families. In the {111} grain family the relative activity between slip systems remains consistent, instead, the intragranular stresses have influenced the magnitude of the shear strains within the slip systems. However, in the {220} grain family the magnitudes of shear strain and the relative activity of slip systems is altered through the influence of intragranular stress. This is particularly evident in the (111)[0-11] slip system which goes from the third most active slip system when no intragranular stress is included to one of the least most active when intragranular stress is included. This highlights the influence the evolving intragranular stress has on neighbouring grain interactions.

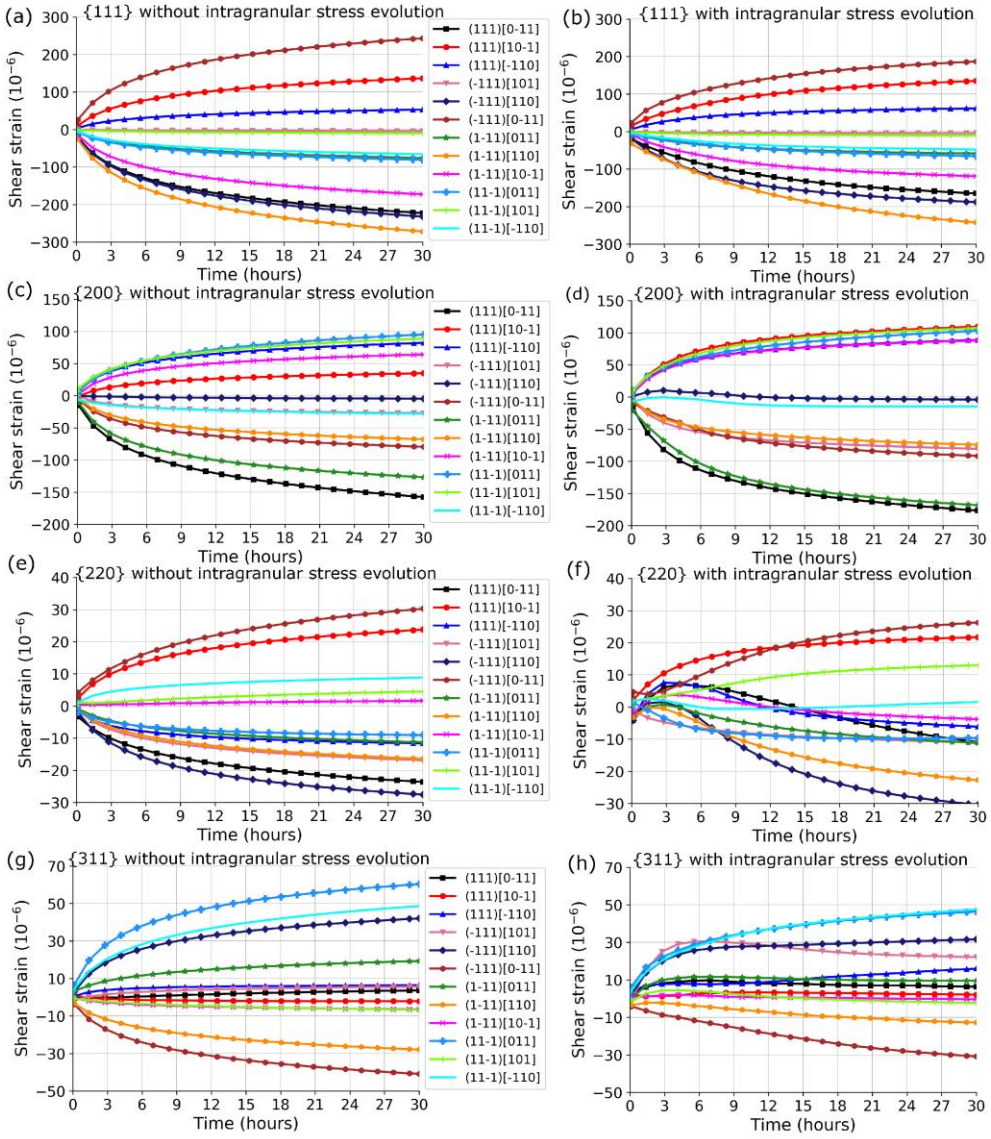

Figure 19 The evolution of shear strain on each slip system during the dwell averaged across each grain family with plane normal orientated in the loading direction. (a), (c), (e), and (g) show the evolution of shear strain with intragranular stress removed from the constitutive model. (b), (d), (f), and (h) show the evolution of shear strain with the intragranular stress included in the constitutive model.

To investigate the influence of the intragranular stress further, the intergranular strains during the load-up and dwell with and without intragranular stress evolution included in the constitutive model is provided in Figure 20. The intergranular strains are calculated by taking the difference between the predicted lattice strains and the ideal elastic case (calculated using Eq. 18). This provides an indication of the plastic intergranular strain due to the competing internal push and pull between grains during deformation. From Figure 20 the influence of the intragranular stress on the predicted intergranular strains is apparent from the difference in evolution in the {220}

and {200} grain families during load-up and all four grain families during the dwell. This suggests that the intragranular stress in the constitutive model has a pronounced influence on the grain environment not only during load-up but also during the dwell. Therefore, deeper insight is required to develop a more comprehensive understanding of how intragranular stress should evolve to ensure its impact on grain-to-grain interactions is accurately represented.

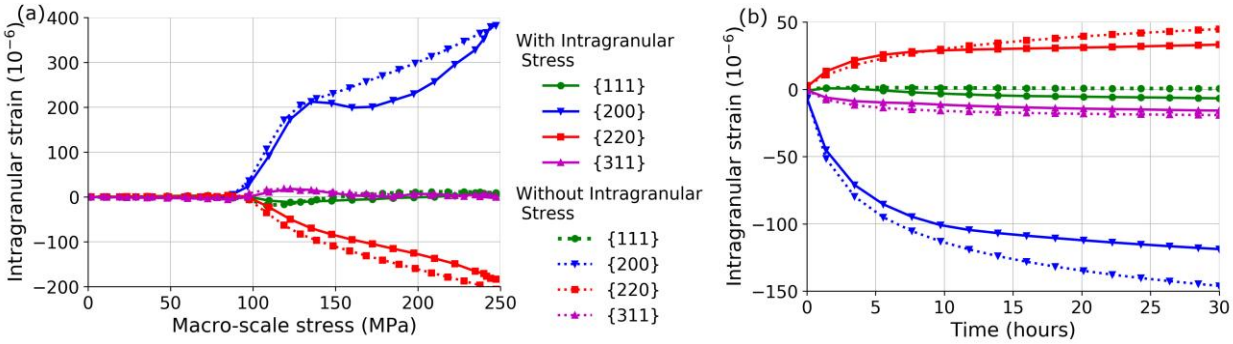

Figure 20 evolution of the intergranular strains during the initial load-up (a) and the strain dwell (b) predicted with and without including intragranular stress in the constitutive model.

8. Conclusion

A constitutive model which combines the deformation evolution during both time independent and time dependent plasticity has been presented. The conception of the model originates from the need to recognise the differing micromechanics occurring in the two regimes and the need to ensure the deformation with each of the regimes correctly influences the deformation of succeeding loading. The following conclusions can be drawn from this study:

1. The superposition of power laws to recognise the differing micromechanics occurring between the load-up and dwell regimes provided ease of transition to occur from time independent and time dependent plasticity during the multiple dwell simulations. The accuracy in simulated relaxation for later dwells also highlighted the model's capability to recognise prior deformation on succeeding load cases.
2. Improvements in simulation accuracy of strain-controlled dwells of 316H at 550°C were achieved through the addition of a recovery component to the evolution of slip hardening. Comparisons made between the experiments and simulations demonstrated the importance of balancing the hardening and recovery during long strain-dwells (>1000 hours).
3. Meso-scale validation of the model highlighted its capability to simulate lattice strain evolution in both the load-up and the dwell, which further supports the presented superposition of power laws to simulate slip. Plastic anisotropy was successfully simulated for each grain family, with deviation from the ideal elastic line for each grain family showing the same trend and magnitude as that in the experimental data. Additionally, the simulation results showed a difference in lattice strain evolution during a load-control dwell compared to a strain-control dwell, a phenomenon also experimentally observed.
4. The evolution of intragranular stress was also shown to influence the predicted intergranular strains during both the load-up and strain-control dwell. This suggests the inclusion of

intragranular stress within the constitutive model will have pronounced influence on the predicted grain-to-grain interactions occurring in the material. This highlights the importance of finding appropriate means of calibrating intragranular stress evolution to ensure the meso-scale environment is accurately represented.

Data availability

The raw experimental data used to compare against simulation results can be obtained from [9, 32-34].

Acknowledgments

The authors would like to thank EDF Energy and EPSRC [grant EP/R020108/1] for funding this work. Additionally, the authors would like to thank the computational facilities of the Advanced Computing Research Centre, University of Bristol (http://www.bris.ac.uk/arc/), which was used for the simulation component of this study. Dr. Wang would also like to acknowledge the RCUK Energy Programme [grant EP/T012250/1] and the UK Government Department for Business, Energy and Industrial Strategy.

Appendix. A. Integration Scheme Applied to the Constitutive Relations

As outlined by Huang [40], the integration scheme implemented in the subroutine is the tangent modulus method for rate dependent solids proposed by Peirce, et al. [93]. Firstly, the increment of shear strain within a time increment Δt is calculated as:

$$\Delta\gamma^{\alpha} = \gamma^{\alpha}(t+\Delta t) - \gamma^{\alpha}(t) \tag{A.127}$$

Employing a linear interpolation with Δt, the increment of shear strain can be calculated,

$$\Delta\gamma^{\alpha}_{t+\Delta t} = \dot{\gamma}^{\alpha}_{t+\Delta t}(\Delta\gamma^{\alpha}_{t+\Delta})\Delta t \tag{A.2}$$

where $\dot{\gamma}^{\alpha}$ is the slip rate in slip system α at time $t+\Delta t$ which is calculated using the following,

$$\dot{\gamma}^{\alpha}_{t+\Delta t} = \left[\dot{\gamma}_{0,1}\left(\frac{|\tau^{\alpha}_{t+\Delta t} - X^{\alpha}_{t+\Delta t}|}{g^{\alpha}_{t+\Delta t}}\right)^{n_1} + \dot{\gamma}_{0,2}\left(\frac{|\tau^{\alpha}_{t+\Delta t} - X^{\alpha}_{t+\Delta t}|}{g^{\alpha}_{t+\Delta t}}\right)^{n_2}\right] sgn(\tau^{\alpha}_{t+\Delta t} - X^{\alpha}_{t+\Delta t}) \tag{A.3}$$

The values for the resolved shear stress, intragranular stress and slip hardening/recovery can be calculated at $t+\Delta t$ once $\Delta\gamma^{\alpha}_{t+\Delta t}$ is known. Firstly, the slip hardening and intergranular stress can be calculated applying the following,

$$g^{\alpha}_{t+\Delta t} = g^{\alpha}_{t} + h_0 \sum_{\beta=1}^{N_s}\left\{\left(1 + \frac{h_0\gamma_{sum(t+\Delta t)}}{\tau_0 m}\right)^{m-1}\left|\Delta\gamma^{\beta}_{t+\Delta t}\right|\right\} - A g_t^{\alpha h}\, exp\left(-\frac{Q}{RT}\right) \tag{A.4}$$

$$X^{\alpha}_{t+\Delta t} = X^{\alpha}_{t} + h\Delta\gamma^{\alpha}_{t+\Delta t} + h_D X^{\alpha}_{t}|\Delta\gamma^{\alpha}_{t+\Delta t}|$$

where the accumulated shear strain ($\gamma_{sum(t+\Delta t)}$) is calculated in the following way,

$$\gamma_{sum(t+\Delta t)} = \gamma^{\alpha}_{t} + \sum_{\alpha}|\Delta\gamma^{\alpha}_{t+\Delta t}| \tag{A.5}$$

The resolved shear stress at $t+\Delta t$ can also be calculated using the shear stress derived in Huang [40], which is given as,

$$\tau^{\alpha}_{t+\Delta \mathrm{t}} = \tau^{\alpha}_{t} + \left[L_{ijkl}\mu^{\alpha}_{kl} + \omega^{\alpha}_{ik}\sigma_{jk(t+\Delta t)} + \omega^{\alpha}_{jk}\sigma_{ik(t+\Delta t)}\right] \cdot \left[\Delta\varepsilon_{ij(t+\Delta t)} - \sum_{\beta}\mu^{\beta}_{ij}\Delta\gamma^{\beta}_{t+\Delta t}\right] \tag{A.6}$$

where L_{ijkl} is the elastic moduli, and μ^{α}_{ij} and ω^{α}_{ij} are given as,

$$\mu^{\alpha}_{\mathrm{ij}} = \frac{1}{2}\left[s_i^{*\alpha}m_j^{*\alpha} + s_j^{*\alpha}m_i^{*\alpha}\right]$$
$$\omega^{\alpha}_{\mathrm{ij}} = \frac{1}{2}\left[s_i^{*\alpha}m_j^{*\alpha} - s_j^{*\alpha}m_i^{*\alpha}\right] \tag{A.7}$$

To calculate the shear rate, Eq 6 must be solved for $\dot{\gamma}$ within an increment of time defined by the step size increment in the FE model. Since Eq 6 is a nonlinear equation containing function of

resolved shear stress (τ^{α}), slip hardening strength (g^{α}) and intragranular stress (X^{α}), a Newton-Raphson scheme was employed to solve for the current slipping rate within the specified time. To distinguish between $\Delta\gamma^{\alpha}$ and the Newton-Raphson iterated version, the $\boldsymbol{\Delta\gamma}^{k}$ is used where k represents the iteration of the Newton-Raphson algorithm. Therefore, the Newton-Raphson iteration is as follows,

$$\boldsymbol{\Delta\gamma}^{\boldsymbol{k+1}} = \boldsymbol{\Delta\gamma}^{k} - \frac{\boldsymbol{R}(\Delta\gamma^{\alpha}_{t+\Delta t})}{\frac{\partial \boldsymbol{R}(\Delta\gamma^{\alpha}_{t+\Delta t})}{\partial \boldsymbol{\Delta\gamma}}} \tag{A.8}$$

where the function to iteratively solve is as follows,

$$\boldsymbol{R}(\Delta\gamma^{\alpha}_{t+\Delta t}) = \Delta\gamma^{\alpha}_{t+\Delta t} - \dot{\gamma}^{\alpha}_{t+\Delta t}(\Delta\gamma^{\alpha}_{t+\Delta})\Delta t \tag{A.9}$$

The solution is arrived at once the following condition is met,

$$|\boldsymbol{R}(\Delta\gamma^{\alpha}_{t+\Delta t})| \leq TOL \tag{A.1028}$$

where the TOL in this study was taken as 1×10^{-6}.

The partial derivate of Eq A.9 with respect to the unknown increment in slip rate ($\partial \boldsymbol{R}(\Delta\gamma^{\alpha}_{t+\Delta t})/\partial \boldsymbol{\Delta\gamma}$) can be calculated using the following equation,

$$\frac{\partial \boldsymbol{R}(\Delta\gamma^{\alpha}_{t+\Delta t})}{\partial \boldsymbol{\Delta\gamma}^{\beta}} = \delta_{\alpha\beta} - \frac{\partial \dot{\gamma}^{\alpha}}{\partial \Delta\gamma^{\beta}}\Delta t \tag{A.11}$$

where $\delta_{\alpha\beta}$ is the Kronecker delta and the partial derivative of the slip rate can be solved following the expression,

$$\frac{\partial \dot{\gamma}^{\alpha}}{\partial \Delta\gamma^{\beta}} = \frac{\partial \dot{\gamma}^{\alpha}}{\partial \tau^{\alpha}}\frac{\partial \tau^{\alpha}}{\partial \Delta\gamma^{\beta}} + \frac{\partial \dot{\gamma}^{\alpha}}{\partial g^{\alpha}}\frac{\partial g^{\alpha}}{\partial \Delta\gamma^{\beta}} + \frac{\partial \dot{\gamma}^{\alpha}}{\partial X^{\alpha}}\frac{\partial X^{\alpha}}{\partial \Delta\gamma^{\alpha}} \tag{A.12}$$

Each of the partial derivatives of slip rate ($\dot{\gamma}^{\alpha}$) with respect to resolved shear stress, slip hardening and intragranular stress can be calculated as,

$$\frac{\partial \dot{\gamma}^{\alpha}}{\partial \tau^{\alpha}} = \frac{1}{g^{\alpha}}\left[\dot{\gamma}_{0,1}n_1\left(\frac{|\tau^{\alpha} - X^{\alpha}|}{g^{\alpha}}\right)^{n_1-1} + \dot{\gamma}_{0,2}n_2\left(\frac{|\tau^{\alpha} - X^{\alpha}|}{g^{\alpha}}\right)^{n_2-1}\right]$$

$$\frac{\partial \dot{\gamma}^{\alpha}}{\partial g^{\alpha}} = -\frac{|\tau^{\alpha} - X^{\alpha}|}{g^{\alpha 2}}\left[\dot{\gamma}_{0,1}n_1\left(\frac{|\tau^{\alpha} - X^{\alpha}|}{g^{\alpha}}\right)^{n_1-1} + \dot{\gamma}_{0,2}n_2\left(\frac{|\tau^{\alpha} - X^{\alpha}|}{g^{\alpha}}\right)^{n_2-1}\right] sgn(\tau^{\alpha} - X^{\alpha}) \tag{A.13}$$

$$\frac{\partial \dot{\gamma}^{\alpha}}{\partial X^{\alpha}} = -\frac{1}{g^{\alpha}}\left[\dot{\gamma}_{0,1}n_1\left(\frac{|\tau^{\alpha} - X^{\alpha}|}{g^{\alpha}}\right)^{n_1-1} + \dot{\gamma}_{0,2}n_2\left(\frac{|\tau^{\alpha} - X^{\alpha}|}{g^{\alpha}}\right)^{n_2-1}\right]$$

Additionally, the partial derivatives for the resolved shear stress, slip hardening and intragranular stress with respect to $\partial\Delta\gamma^{\beta}$ can be calculated as,

$$\frac{\partial \tau^{\alpha}}{\partial \Delta\gamma^{\beta}} = \sum_{\beta} \mu^{\beta}_{ij}\left[L_{ijkl}\mu^{\alpha}_{kl} + \omega^{\alpha}_{ik}\sigma_{jk} + \omega^{\alpha}_{jk}\sigma_{ik}\right] \tag{A.14}$$

$$\frac{\partial g^{\alpha}}{\partial \Delta\gamma^{\beta}} = h_0 \sum_{\beta=1}^{N_s} \left\{ \left(1 + \frac{h_0 \gamma_{sum(t+\Delta t)}}{\tau_0 m} \right)^{m-1} sgn\left(\Delta\gamma^{\beta}\right) \right\}$$

$$\frac{\partial X^{\alpha}}{\partial \Delta\gamma^{\beta}} = h\delta_{\alpha\beta} - h_D X^{\alpha} \delta_{\alpha\beta} sgn(\Delta\gamma^{\alpha})$$

Using the equations in Eq A.13 and Eq A.14, the partial derivative in Eq A.12 can be solved and finally, the value of $\boldsymbol{\Delta\gamma^{k+1}}$ can be solved.

References

[1] S. Tin, M. Detrois, J. Rotella, M.D. Sangid, JOM, 70 (2018) 2485-2492.
[2] C.C. Tasan, J.P.M. Hoefnagels, M. Diehl, D. Yan, F. Roters, D. Raabe, International Journal of Plasticity, 63 (2014) 198-210.
[3] S. Sinha, J.A. Szpunar, N.A.P. Kiran Kumar, N.P. Gurao, Materials Science and Engineering: A, 637 (2015) 48-55.
[4] G. Song, Z. Sun, L. Li, X. Xu, M. Rawlings, C.H. Liebscher, B. Clausen, J. Poplawsky, D.N. Leonard, S. Huang, Z. Teng, C.T. Liu, M.D. Asta, Y. Gao, D.C. Dunand, G. Ghosh, M. Chen, M.E. Fine, P.K. Liaw, Scientific Reports, 5 (2015).
[5] M.P. Petkov, J. Hu, A.C.F. Cocks, Philosophical Magazine, (2018) 1-46.
[6] T.D. Joseph, D. McLennon, M.W. Spindler, C.E. Truman, D.J. Smith, Materials at High Temperatures, 30 (2013) 156-160.
[7] S. Kikuchi, B. Ilschner, Scripta Metallurgica, 20 (1986) 159-162.
[8] A. Fookes, S.X. Li, D.J. Smith, M.W. Spindler, in: 2nd ECCC International Conference on Creep and Fracture in High Temperature Componets: Design and Life Assessment Issues, 2009.
[9] A.A. Mamun, C. Simpson, D. Agius, C. Reinhard, C. Truman, M. Mostafavi, D. Knowles, Acta Materialia, (In Review) (2019).
[10] A.A. Mamun, R.J. Moat, J. Kelleher, P.J. Bouchard, Materialia, 7 (2019) 100385.
[11] A. A. Mamun, R.J. Moat, J. Kelleher, P.J. Bouchard, Materials at High Temperatures, 31 (2014) 378-382.
[12] A.A. Mamun, C. Simpson, T. Erinosho, D. Agius, C. Reinhard, M. Mostafavi, D. Knowles, in: ASME 2019 Pressure Vessels & Piping Conference, San Antonio, TX, USA, 2019.
[13] J. Hu, A.C.F. Cocks, International Journal of Solids and Structures, 78-79 (2016) 21-37.
[14] H. Wang, B. Clausen, C.N. Tomé, P.D. Wu, Acta Materialia, 61 (2013) 1179-1188.
[15] J.N. Hu, A.C.F. Cocks, Scripta Materialia, 128 (2017) 100-104.
[16] B. Chen, J.N. Hu, P.E.J. Flewitt, A.C.F. Cocks, R.A. Ainsworth, D.J. Smith, D.W. Dean, F. Scenini, Materials at High Temperatures, 32 (2015) 592-606.
[17] H. Wang, Y. Jeong, B. Clausen, Y. Liu, R.J. McCabe, F. Barlat, C.N. Tomé, Materials Science and Engineering: A, 649 (2016) 174-183.
[18] D.-F. Li, C.M. Davies, S.-Y. Zhang, C. Dickinson, N.P. O'Dowd, Acta Materialia, 61 (2013) 3575-3584.
[19] Y. Guilhem, S. Basseville, F. Curtit, J.M. Stéphan, G. Cailletaud, International Journal of Fatigue, 32 (2010) 1748-1763.
[20] L. Signor, P. Villechaise, T. Ghidossi, E. Lacoste, M. Gueguen, S. Courtin, Materials Science and Engineering: A, 649 (2016) 239-249.
[21] K. Minaii, G.H. Farrahi, M. Karimpour, H. Bahai, G.H. Majzoobi, Fatigue and Fracture of Engineering Materials and Structures, 42 (2019) 640-650.
[22] A. Guery, F. Hild, F. Latourte, S. Roux, International Journal of Plasticity, 81 (2016) 249-266.
[23] J. Hure, S. El Shawish, L. Cizelj, B. Tanguy, Journal of Nuclear Materials, 476 (2016) 231-242.
[24] D.-F. Li, N.P. O'Dowd, C.M. Davies, S.-Y. Zhang, European Journal of Mechanics - A/Solids, 30 (2011) 748-760.
[25] D.-F. Li, N.P. O'Dowd, Journal of the Mechanics and Physics of Solids, 59 (2011) 2421-2441.
[26] D. Gonzalez, J.F. Kelleher, J. Quinta da Fonseca, P.J. Withers, Materials Science and Engineering: A, 546 (2012) 263-271.
[27] B. Chen, J.N. Hu, P.E.J. Flewitt, D.J. Smith, A.C.F. Cocks, S.Y. Zhang, Acta Materialia, 67 (2014) 207-219.
[28] B. Chen, J.N. Hu, Y.Q. Wang, S.Y. Zhang, S. Van Petegem, A.C.F. Cocks, D.J. Smith, P.E.J. Flewitt, Acta Materialia, 85 (2015) 229-242.

[29] S. Hasunuma, T. Ogawa, International Journal of Fatigue, 127 (2019) 488-499.
[30] M.P. Petkov, J. Hu, E. Tarleton, A.C.F. Cocks, International Journal of Solids and Structures, 171 (2019) 54-80.
[31] T.O. Erinosho, K.A. Venkata, M. Mostafavi, D.M. Knowles, C.E. Truman, International Journal of Solids and Structures, 139-140 (2018) 129-137.
[32] Y.Q. Wang, M.W. Spindler, C.E. Truman, D.J. Smith, Materials & Design, 95 (2016) 656-668.
[33] Y.Q. Wang, H.E. Coules, C.E. Truman, D.J. Smith, International Journal of Solids and Structures, 135 (2018) 219-232.
[34] Y.Q. Wang, S. Hossain, S. Kabra, S.Y. Zhang, D.J. Smith, C.E. Truman, Journal of Materials Science, 52 (2017) 7929-7936.
[35] G.I. Taylor, Journal of the Institute of Metals, 62 (1938) 307-324.
[36] R. Hill, Journal of the Mechanics and Physics of Solids, 14 (1966) 95-102.
[37] J.R. Rice, Journal of the Mechanics and Physics of Solids, 19 (1971) 433-455.
[38] R. Hill, J.R. Rice, Journal of the Mechanics and Physics of Solids, 20 (1972) 401-413.
[39] S. Sadik, A. Yavari, Mathematics and Mechanics of Solids, (2015).
[40] Y. Huang, in, Division of Applied Sciences, Harvard University, Cambridge, Massachusetts, 1991.
[41] W. Hutchinson John, R. Hill, Proceedings of the Royal Society of London. A. Mathematical and Physical Sciences, 348 (1976) 101-127.
[42] R.J. Asaro, A. Needleman, Acta Metallurgica, 33 (1985) 923-953.
[43] M. Ghorbani Moghaddam, A. Achuthan, B.A. Bednarcyk, S.M. Arnold, E.J. Pineda, Materials Science and Engineering: A, 703 (2017) 521-532.
[44] D. Peirce, R.J. Asaro, A. Needleman, Acta Metallurgica, 30 (1982) 1087-1119.
[45] B.S. Fromm, K. Chang, D.L. McDowell, L.Q. Chen, H. Garmestani, Acta Materialia, 60 (2012) 5984-5999.
[46] J. Hu, B. Chen, D.J. Smith, P.E.J. Flewitt, A.C.F. Cocks, International Journal of Plasticity, 84 (2016) 203-223.
[47] P.J. Armstrong, C.O. Frederick, in: G.E.G.B. Report RD/B/N, Central Electricity Generating Board, 1966.
[48] B.D. Smith, D.S. Shih, D.L. McDowell, International Journal of Plasticity, 101 (2018) 1-23.
[49] A.S. Khan, P. Cheng, International Journal of Plasticity, 12 (1996) 147-162.
[50] R.D. McGinty, D.L. McDowell, Journal of Engineering Materials and Technology, 121 (1999) 203-209.
[51] M.F. Horstemeyer, D.L. McDowell, Mechanics of Materials, 27 (1998) 145-163.
[52] B. Xu, Y. Jiang, International Journal of Plasticity, 20 (2004) 2161-2178.
[53] W.J. Duffin, F.A. Nichols, Journal of Nuclear Materials, 45 (1973) 302-316.
[54] A. Staroselsky, B.N. Cassenti, Mechanics of Materials, 42 (2010) 945-959.
[55] A. Staroselsky, B.N. Cassenti, International Journal of Solids and Structures, 48 (2011) 2060-2075.
[56] D. Leidermark, M. Segersäll, Computational Materials Science, 90 (2014) 61-70.
[57] R.A. Lebensohn, C.S. Hartley, C.N. Tomé, O. Castelnau, Philosophical Magazine, 90 (2010) 567-583.
[58] M. Shenoy, Y. Tjiptowidjojo, D. McDowell, International Journal of Plasticity, 24 (2008) 1694-1730.
[59] M.M. Shenoy, A.P. Gordon, D.L. McDowell, R.W. Neu, Journal of Engineering Materials and Technology, 127 (2005) 325-336.
[60] R.W. Bailey, Journal of the Institute of Metals, 35 (1926) 27-40.
[61] E. Orowan, Journal of the West of Scotland Iron and Steel Institute, 54 (1946) 45-53.
[62] L. Shi, D.O. Northwood, Acta Metallurgica et Materialia, 42 (1994) 871-877.
[63] L.N. McCartney, The Philosophical Magazine: A Journal of Theoretical Experimental and Applied Physics, 33 (1976) 689-695.
[64] J.H. Gittus, The Philosophical Magazine: A Journal of Theoretical Experimental and Applied Physics, 23 (1971) 1281-1296.

[65] R.W. Evans, B. Wilshire, Introduction to Creep, The Institute of Materials, London, 1993.
[66] J. Harder, International Journal of Plasticity, 15 (1999) 605-624.
[67] H. Conrad, J. Narayan, Scripta materialia, 11 (2000) 1025-1030.
[68] H.H. Fu, D.J. Benson, M.A. Meyers, Acta Materialia, 49 (2001) 2567-2582.
[69] DREAM3D, in, http://dream3d.bluequartz.net/, 2018.
[70] DassaultSystèmes, in, 2018.
[71] R.K. Verma, P. Biswas, Materials Science and Technology (United Kingdom), 32 (2016) 1553-1558.
[72] R. Voothaluru, C.R. Liu, Fatigue and Fracture of Engineering Materials and Structures, 37 (2014) 671-681.
[73] M. Naderi, M. Amiri, N. Iyyer, P. Kang, N. Phan, Fatigue & Fracture of Engineering Materials & Structures, 39 (2015) 167-179.
[74] Z. Zhang, M.A. Cuddihy, F.P.E. Dunne, Proceedings of the Royal Society A: Mathematical, Physical and Engineering Sciences, 471 (2015).
[75] R.J. Kashinga, L.G. Zhao, V.V. Silberschmidt, F. Farukh, N.C. Barnard, M.T. Whittaker, D. Proprentner, B. Shollock, G. McColvin, Materials Science and Engineering: A, 708 (2017) 503-513.
[76] A.H. Cottrell, Dislocations and plastic flow in crystals, Clarendon, Oxford, England, 1953.
[77] F.J. Harewood, P.E. McHugh, Computational Materials Science, 39 (2007) 481-494.
[78] L. Kloc, V. Skienička, J. Ventruba, Materials Science and Engineering: A, 319-321 (2001) 774-778.
[79] T. Eiter, H. Mannila, in, Information Systems Department, Technical University of Vienna, 1994.
[80] M.M. Fréchet, Rendiconti del Circolo Matematico di Palermo (1884-1940), 22 (1906) 1-72.
[81] A.F. Saleeb, S.M. Arnold, International Journal of Plasticity, 20 (2004) 2111-2142.
[82] J. Douglas, M. Spindler, R. Dennis, in: 2007 Proceedings of the ASME Pressure Vessels and Piping Conference - 8th International Conference on Creep and Fatigue at Elevated Temperatures - CREEP8, 2008, pp. 399-418.
[83] B. Chen, J.N. Hu, Y.Q. Wang, S. Kabra, A.C.F. Cocks, D.J. Smith, P.E.J. Flewitt, Journal of Materials Science, 50 (2015) 5809-5816.
[84] A. Al Mamun, C. Simpson, D. Agius, T.L. Lee, S. Kabra, C. Truman, M. Mostafavi, D. Knowles, Materials Science and Engineering: A, (2020) 139374.
[85] W.D. Musinski, D.L. McDowell, International Journal of Mechanical Sciences, 100 (2015) 195-208.
[86] R. Pokharel, A. Patra, D.W. Brown, B. Clausen, S.C. Vogel, G.T. Gray, International Journal of Plasticity, 121 (2019) 201-217.
[87] D. Agius, M. Kajtaz, K.I. Kourousis, C. Wallbrink, W. Hu, Aircraft Engineering and Aerospace Technology, 90 (2018) 251-260.
[88] D. Agius, M. Kajtaz, K.I. Kourousis, C. Wallbrink, C.H. Wang, W. Hu, J. Silva, Materials & Design, 118 (2017) 107-121.
[89] U.F. Kocks, Metallurgical and Materials Transactions, 1 (1970) 1121-1143.
[90] J. Hu, G. Green, S. Hogg, R. Higginson, A. Cocks, Materials Science and Engineering: A, 772 (2020) 138787.
[91] Y. Dong, T. Nogaret, W.A. Curtin, Metallurgical and Materials Transactions A, 41 (2010) 1954-1960.
[92] J. Wang, M. Zecevic, M. Knezevic, I.J. Beyerlein, International Journal of Plasticity, 125 (2020) 294-313.
[93] D. Peirce, C.F. Shih, A. Needleman, Computers & Structures, 18 (1984) 875-887.